Flow physics during the drying of a thin polymer solution film near the contact line

by

Ashkan Babaie

A THESIS SUBMITTED IN PARTIAL FULFILLMENT OF THE REQUIREMENTS FOR THE DEGREE OF

DOCTOR OF PHILOSOPHY

in

THE FACULTY OF GRADUATE AND POSTDOCTORAL STUDIES
(Mechanical Engineering)

The University of British Columbia
(Vancouver)

August 2015

Abstract

The drying process of a thin polymer solution film has been studied inside a micro-liter cavity near the contact line. Confocal microscopy along with particle image velocimetry and laser induced fluorescence are used for the real time measurement of velocity and concentration fields during the drying process.

In addition to the capillary flow and the Marangoni flow, the velocity field also reveals the possible existence of a single vortex and multiple vortices inside the creeping flow induced by evaporation. These vortices appear soon after the beginning of the evaporation process, their size shrinks over time, and they disappear before the end of the evaporation process. This thesis includes a study of the effect of rheological and geometrical parameters on the presence, size and endurance of these vortices.

Significant concentration heterogeneity is observed across the film during the drying process, in particular near the contact line. The concentration at the solution-air interface is higher compared to the bulk, and it increases towards the

contact line and also over time. A skin layer starts forming as soon as the surface concentration reaches the glass transition concentration after which the evaporation rate starts decreasing. The drying film undergoes a similar concentration evolution during the evaporation process, regardless of the cavity depth and the initial polymer concentration; although, minor differences can be recognized that are associated with the flow recirculations that delay the concentration increase inside the vortex.

Finally, a theory is developed based on experimental data which explains the existence and behavior of viscous vortices near the bottom wall of the cavity. The competition between the capillary flow and the Marangoni flow results in flow separation on the bottom wall which leads to such vortices.

This study provides better understanding of the drying process of thin polymer solution films near the contact line. Furthermore, viscous flow separation adds to the current understanding of flow physics during the drying process, in addition to the well-known evaporation induced capillary transport and the Marangoni effect.

Preface

This PhD thesis entitled "Flow physics during the drying of a thin polymer solution film near the contact line" represents original research carried out by the author, Ashkan Babaie, during his PhD studies under supervision of Prof. Boris Stoeber at the University of British Columbia. The experiments were performed mostly at the BioMEMS lab in the Advanced Materials and Process Engineering Laboratory (AMPEL) and at the Walus Lab at the Lower Mall Research Station (LMRS) at UBC. This study was funded through UBC's Four Year Doctoral Fellowship program and a Collaborative Health Research Program (CHRP) grant from the Natural Science and Engineering Council (NSERC) and the Canadian Institute for Health Research (CIHR). The contributions published or submitted from the current studies are mentioned in this preface.

A version of Chapter 2 has been published as, *A. Babaie, S. Madadkhani, and B. Stoeber, "Evaporation-driven low Reynolds number vortices in a cavity," Phys. Fluids, vol. 26, no. 3, art. no. 033102, Mar. 2014*. I performed most of the

experiments and analysis and prepared the manuscript. In addition, S. Madadkhani helped with viscometry experiments and Prof. B. Stoeber helped with data analysis, discussions and preparation of the final version of the manuscript.

A version of Chapter 3 has been published as *A. Babaie and B.Stoeber, "Concentration Field Evolution during the Drying of a Thin Polymer Solution Film near the Contact Line." Langmuir, vol 31, Aug 2015*. I conducted this study by performing all the experiments and data analysis and prepared a manuscript. Prof. B. Stoeber helped with discussions, data analysis and preparation of the final version of the manuscript.

A version of Chapter 4 has been published as *A. Babaie and B. Stoeber, "Viscous flow separation caused by the Marangoni effect in competition with capillary flow," Phys. Fluids, vol. 27, no. 7, p. 071702, Jul. 2015*. I performed this study by doing all the theoretical analysis and prepared the manuscript. Prof. B. Stoeber helped with preparation of the final version of the manuscript.

Table of contents

List of figures

Acknowledgements

First of all, I would like to thank my supervisor, Prof. Boris Stoeber, for all his help and support during my PhD studies. He has always been there for me, and I could not have imagined any better supervisor. His inspiration, professional guidance and patience helped me enjoy every moment while working on this thesis. I also thank the University of British Columbia for financial support through the Four Year Doctoral Fellowship program.

I thank my PhD proposal committee Prof. Ian Frigaard, Prof. Dana Grecov and Prof. Savvas Hatzikiriakos for their constructive feedback and advice during proposal committee meetings. I also thank Prof. Karen Cheung, Prof. Konrad Walus and Prof. Mu Chiao for allowing me to use their lab spaces and equipment.

I am grateful to my lab mates and friends at Stoeber Lab, especially Dr. Iman Mansoor, Dr. Vahid Bazargan and Nathan Wolfe for all their kind help, advice and technical training throughout this project.

Living four years far away from the home and family has its own challenges and difficulties and could not have been possible without encouragement and support of my lovely friends in Vancouver, Shadi Assadi, Moein Javadian, Sina Amini, Maryam Eslami, Dr. Amin Rahmani and Farzad Hemmati.

Finally, my debt of gratitude is to my Mom, Dr. Salehian, my Dad, Dr. Babaie, and my successful sister Saina who have supported me with their unconditional love and their patience during my absence.

Dedication

To my grandfather

who was a school teacher and

dedicated his life to children education

1 Introduction

1.1 Motivation

Precise polymer deposition through the controlled drying of a polymer solution is used for a variety of applications in different industries. Inkjet printing and solvent casting of polymer solutions are two key technologies used for this purpose. Manufacturing of polymer light-emitting diode (PLED) displays [1], printing circuits [2], fabrication of electronic components such as transistors [3], and microlens fabrication [4][5] are applications of controlled polymer deposition through inkjet printing.

Solvent casting on the other hand is the oldest technology for polymer deposition and was used initially in the photographic industry [6]. It requires a polymer soluble in a volatile solvent such as water in order to make a stable solution. The solution typically forms a homogeneous film after drying that is then released from the cast [6]. This technique is used for the production of different products such as photographic films, synthetic fibers, adhesives, etc. [7].

Polyvinyl alcohol (PVA), as a water soluble polymer is widely used in solvent casting processes due to its physical and chemical properties. High tensile strength, barrier to oxygen and resistance to abrasion are some of the properties of PVA films. PVA is made by hydrolysis of polyvinyl acetate and its physical properties depend on the hydrolysis process and its molecular weight [8]. Solvent casting of PVA solutions is used in a variety of applications such as the manufacturing of LCD displays [6], the fabrication of contact lenses [9] and the fabrication of micro-needles for painless drug delivery [10].

The fabrication of microneedles through solvent casting of PVA solutions [10] is shown in Fig. 1-1. The casting process starts with loading the PVA solution into a mold including vertical pillars. As the solvent (water) evaporates from the solution, the PVA starts depositing in a volcanic shape around the pillars and in a similar way around the cavity's side walls. The deposited PVA layer is then separated from the mold by mechanical or chemical means.

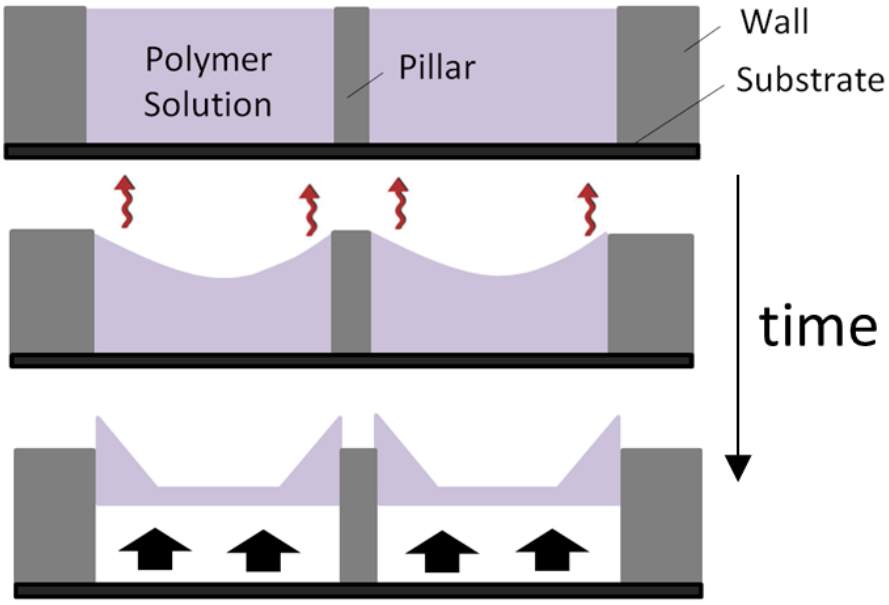

Figure 1-1 Solvent casting process for fabrication of microneedles

Structural and molecular non-uniformities have been observed across the deposited film depending on the drying condition [11]. These non-uniformities are mostly caused by non-uniform polymer transport and non-homogeneous drying across the film. Thus, understanding the physics of the drying process is essential for an optimum design of these polymer microstructures; however, this fluid mechanics problem is quite complex, involving a changing flow domain including a highly curved meniscus region and a polymer concentration varying in space and time.

1.2 Literature review

1.2.1 Polyvinyl alcohol

PVA is the largest synthetic water-soluble resin produced in the world based on volume at an industrial scale. It is typically made by hydrolysis of polyvinyl acetate. The degree of hydrolysis of PVA determines the percentage of acetate groups replaced by hydroxyl groups during the reaction process [12].

Different properties of PVA such as solubility, flexibility, and tensile strength depend on the degree of hydrolysis and the molecular weight of PVA [8]. PVA can achieve high crystallinity levels $(20\% - 50\%)$ [13], and the crystallinity level increases for lower molecular weight and at a higher degree of hydrolysis. For PVAs with a high degree of hydrolysis, the hydroxyl groups from different polymer chains bond to each other and produce structural orientation. On the other hand, for larger molecular chains it is more difficult for polymer molecules to align over their entire length and create crystalline structures [14].

PVA is soluble in highly polar and hydrophilic solvents, and water is the most common solvent for PVA. The solubility, viscosity and surface tension of PVA solutions depend on temperature, concentration, degree of hydrolysis and molecular weight. At low molecular weight and with low degree of hydrolysis PVA is fully soluble at room temperature; however, at higher molecular weight

and higher degree of hydrolysis higher temperatures are required to assist with the polymer solubility [8].

The viscosity of polymer solutions is highly affected and increases with the molecular weight and the polymer concentration [15][16]. The surface tension of water is significantly reduced by adding a very small amount of PVA ($< 0.1\, wt\%$), and it then decreases slightly with increasing PVA concentration [17][18].

1.2.2 Drying of polymer solution films

The drying of a flat film of polymer solution has been the topic of theoretical study for many years. Okazaki et al. [19] solved the diffusion transport equations in a drying film of PVA solution using experimental data for the diffusion coefficient. They used a micro-interferometric method to measure mutual diffusion coefficients in different concentrations of aqueous PVA solutions and found the water concentration across the film. In a similar theoretical study for an evaporating thin-film of PVA/toluene solution, Vrentas [20] reported the existence of a significant concentration gradient near the surface due to the skinning effect.

The formation of a layer at the solution-air interface whose properties are significantly different from the properties of the bulk solution is known as the skinning effect. The reason for this effect is a higher surface concentration which

limits diffusional mass transport near the surface [20]. Microscopic dynamical studies performed with imaging techniques such as magnetic resonance imaging (MRI), reveal the formation of a skin layer for thick layers of polymer solution that dried quickly, while thinner layers which are dried slowly have a more uniform concentration profile [21]. The concentration heterogeneity across the film influences the local film structure by changing the level of crystallinity across the film [22]. A glassy skin layer will be formed at the surface due to the lack of immobility, while drying-induced crystallization can occur beneath the skin [23].

1.2.3 The evaporation process near the contact line

The drying process becomes even more complicated at the meniscus [24], as the evaporation-induced convection will affect the polymer transport. For an evaporating film near a vertical wall, the solvent evaporation rate is maximum at the location where the contact line is attached to the wall [25][24]. In order for the contact line to stay pinned to the wall, the capillary flow towards the contact line compensates the excess solvent mass loss at this point [26]. This flow transports additional polymer towards the contact line at the wall. A similar phenomenon is observed during the drying of a colloidal droplet on a flat substrate resulting in the so called “coffee ring effect” [25]. In a drying coffee spill, the capillary flow

towards the contact line takes the coffee particles to the contact line, resulting in a ring-like deposit [27][28].

Due to the capillary transport and non-uniform evaporation at the meniscus, a polymer concentration gradient will exist along the surface. For many polymer solutions, the surface tension is a function of polymer concentration. In particular for aqueous PVA solutions, the surface tension decreases with increasing polymer concentration [8]. As a result, the polymer concentration gradient at the surface leads to a surface tension gradient which generates a flow due to the Marangoni effect [29]. The Marangoni effect generates a flow from a region with low surface tension to a region with high surface tension. In the case of a PVA solution film, the region of low surface tension will be near the contact line where the highest polymer concentration exists. As a result, there will be a Marangoni flow at the surface away from the contact line. The two major transport mechanisms inside an evaporating PVA film beside a vertical wall are shown in Fig. 1-2 [30].

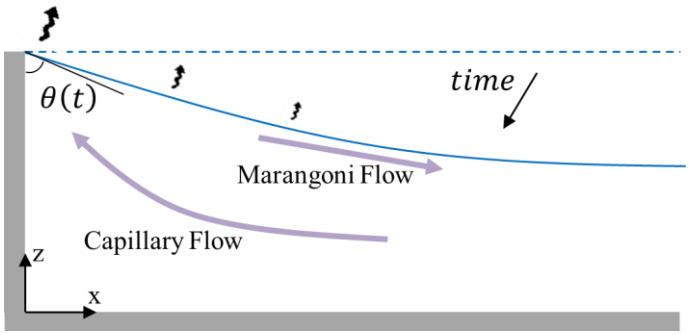

Figure 1-2 Transport mechanisms inside a drying polymer solution

The effect of different transport mechanisms on the final polymer deposition has been studied in the literature. For an evaporating polymer solution inside a cylindrical micro-cavity, Kajiya and Doi [31] used optical microscopy to image the surface profile of the film. They observed excessive polymer deposition near the side walls due to the capillary flow towards the contact line; however, the deposition profile became flat after adding surfactant to the solution as Marangoni flow from the contact line reversed the capillary transport and resulted in a more leveled deposition inside the cavity.

Because of significant effects of transport mechanisms on the shape and structure of the deposited film, it is necessary that the velocity and the concentration fields be known during the drying process and specifically at the meniscus. Yiantsios and Higgins [32] used numerical modelling with thin-film approximation to study the Marangoni effect during the drying of colloidal films. They reported different types of particle coatings based on the Peclet number. For instance at high Peclet numbers, they reported skin layer formation with low concentration fluid remaining beneath the skin.

Chamarthy et al. [33] used 3D micro particle image velocimetry (PIV) to study the thermo-capillary transport of methanol evaporation near the meniscus inside a horizontal capillary tube. They studied the effect of tube diameter on the Marangoni recirculations near the contact line. In a similar study, Buffone et al.

[34] studied the effect of the contact angle on the Marangoni recirculation near the contact line by performing both PIV and infrared temperature measurement. They observed Marangoni recirculations in the same direction for convex, flat and concave surface profiles.

Mansoor and Stoeber [30] visualized the evaporation induced velocity field including the Marangoni effect during the evaporation of a PVA solution inside a cavity near the contact line. They used 3D confocal microscopy and micro PIV to study the effect of temperature on the evaporation-induced flow field.

Although the velocity field has been measured by means of advanced imaging and image processing techniques, the concentration field at the meniscus is not very well known yet. Optical tweezers [35] or electric field tweezers [36] have been used for point measurement of concentration or concentration-dependent properties such as viscosity or surface tension; however, most of these techniques are limited to point measurements at the surface of flat films and are not practical for concentration field measurement near the meniscus.

In a very recent study, Komoda et al. [37] used oscillatory microdisk rheometry to measure the surface viscoelastic properties of a drying aqueous PVA solution at the center of a micro-liter cavity. The surface concentration was then estimated from the measured viscosity and was compared with theoretical results of a simplified 1D diffusion model. Based on this comparison, they found higher local

concentrations near the surface at the beginning, but later in the drying process the polymer concentration becomes uniform across the film.

In the absence of concentration and structural data, the drying of polymer solution films near the meniscus is still not very well understood. Phenomena such as skin formation, which are known from research on flat thin films, are expected to occur at the meniscus as well; however, the concentration values and their variations across the film and during the drying process are not known. In addition, the effect of the evaporation-induced velocity field and different flow parameters on the drying process need to be studied.

1.2.4 Low Reynolds number vortices

Evaporation driven capillary flow and the Marangoni flow are not the only phenomena occurring during the evaporation of a polymer solution inside a microliter well. Low Reynolds number vortices might also be generated by the capillary bulk flow during the evaporation process.

Viscous and resistive eddies near a sharp concave corner were first introduced in 1964 and named after H. K. Moffatt who mathematically predicted these eddies [38]. The governing equation he suggested was the Stokes equation, as $\nabla^4 \psi = 0$ with the stream function ψ. The physical explanation for these low Reynolds number eddies was not reported in this paper; however, it was mentioned that "although viscosity is usually a damping mechanism, it can also be responsible

for the generation of a geometrical progression of eddies". The first experimental visualization of separating Stokes flows was performed by S. Taneda [39]. He provided images of the low Reynolds number (Re~0.01) vortices in different geometries such as the flow past a cavity or the flow past a square bank.

Low Reynolds number vortices have also been observed in gravity-driven film flowing over strongly undulated bottom profiles [40][41][42]. It is reported that there is a direct relationship between the vortex generation and the thickness of the fluid film, and no vortices were observed in films below a certain thickness. Moffatt vortices have also been observed recently for creeping flows in micro-geometries. Oliveira et al. [43] reported the formation of low Reynolds number vortices in creeping Newtonian fluid flows in cross-slot microchannels. They found good agreement between their experimental visualization and numerical simulations and used computational fluid dynamics (CFD) to study the effects of geometry and inertia on the flow behavior. They found that the appearance of the vortices is affected by the geometry and it is enhanced by the increase of the Reynolds number. Most recently, Fishler et al. [44] used both PIV and CFD simulations to analyze flow and vortices in cylindrical micro-cavities inside a microfluidic device at Reynolds numbers around unity (Re = 0.1, 1 and 10). They captured the transition from a non-separating flow to a single vortex and then the transition to recirculation systems with two and three vortices based on the Reynolds number and geometry parameters. The inertial effect was found to

cause a break of symmetry and spatial arrangement of the vortices at Re = 1. Vortices were only seen in either deep cylindrical micro-cavities (tube-like geometries) or in cavities with a small opening. They also found that two- and three-vortex configurations are only formed at a limited range of geometry parameters, typically in deep cavities with small openings.

1.3 Thesis outline

In this thesis, a comprehensive experimental and theoretical study is performed on the drying of a PVA solution film inside a cavity and near the contact line. The drying process is studied in a 2D geometry near the vertical wall. This geometry is different from the microneedle geometry, as there is a 3 dimensional evaporation induced velocity field around a pillar while a 2 dimensional velocity field exists near the vertical wall; however, because of the symmetry, at each vertical plane crossing the center of the pillar, the two dimensional velocity field will be similar to the flow near the vertical wall. In addition, the two dimensional geometry makes it possible to construct a projection image in the vertical plane to improve the signal to noise ratio for the PIV analysis without removing any velocity components.

A velocimetry technique based on the work by Mansoor and Stoeber [30] is used to measure the velocity field in cavities with different heights and for a range of different initial polymer concentrations. A fluorescent-based optical measurement

technique is introduced for concentration field measurements near the meniscus. The effect of different flow parameters on the concentration field across the film are studied over time. Finally, velocity field and concentration field data are combined to develop a theory that explains the newly identified phenomena involved in the drying of polymer solution thin films.

In Chapter 2, a parametric study is performed on the evaporation driven velocity field near the meniscus for a PVA solution. Confocal microscopy and particle image velocimetry are used to measure the velocity field in cavities with different depths and with different initial polymer concentrations. In addition to evaporation-driven flow and Marangoni flow, the velocity field also reveals single and multiple vortices generated within the creeping flow induced by evaporation. The effects of geometry and the rheology of the fluid on the presence, endurance and the size of these vortices are also investigated in this chapter.

In Chapter 3, an experimental study is performed for polymer concentration field measurement during the drying of a thin film in a cavity near the meniscus. Measurements are based on optical techniques such as 3D confocal microscopy and laser-induced fluorescence. Here, again for a range of initial polymer concentrations and for different cavity heights, the polymer concentration field is measured across the film. Defining non-dimensional parameters, it is shown that the concentration field undergoes a similar evolution during the drying process,

regardless of initial concentration or the cavity depth. The effect of the capillary number on the surface concentration is also investigated.

In Chapter 4, experimental data such as surface concentration and the surface profile are used with governing thin-film equations in order to develop a theory that explains the flow recirculation introduced in Chapter 2. The developed model explains the physics of the observed recirculation and predicts the flow separation locations on the bottom wall of the cavity.

Chapter 5 provides a summary of the major findings of this thesis, including the limitations of the methodology, and provides suggestions for future work.

2 Evaporation-driven low Reynolds number vortices

2.1 Introduction

The capillary flow caused by enhanced evaporation near the contact line and the spherical geometry of an evaporating droplet and the Marangoni flow near the free surface have been described in the literature. However, these are not the only phenomena occurring during the evaporation of polymer solutions near the meniscus. Low Reynolds number vortices might also be generated inside the evaporation-driven flow field as shown in Fig. 2-1. In this chapter, we introduce these low Reynolds number vortices that occur inside a cavity filled with an evaporating polymer solution.

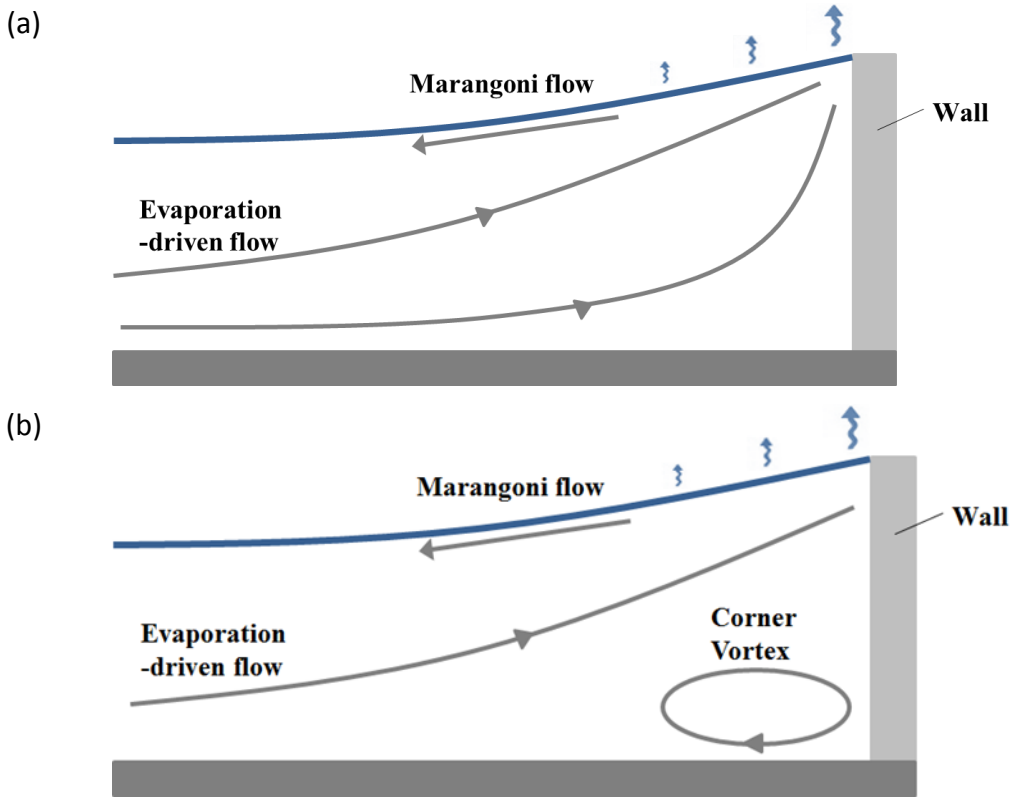

Figure 2-1 Schematic of possible flow phenomena during the evaporation of a polymer solution near a wall inside a well, (a) without the corner recirculation, (b) with a corner recirculation

2.2 The physical problem

The schematic of a drying polymer solution inside a cavity next to a vertical wall is depicted in Fig. 2-2. Assuming the domain is large in the y −direction we will only consider the problem in the x − z plane. As shown, the contact line is pinned at the upper edge of the wall and the contact angle θ is changing with time. The solvent evaporation induces a velocity field inside the film (Fig. 2-2) with a possible formation of a vortex in the corner between the bottom and the wall of

the cavity (Fig. 2-1). As the solvent evaporates the viscosity of the solution increases and after the entire solvent has evaporated a dry polymer coating will remain on the structure.

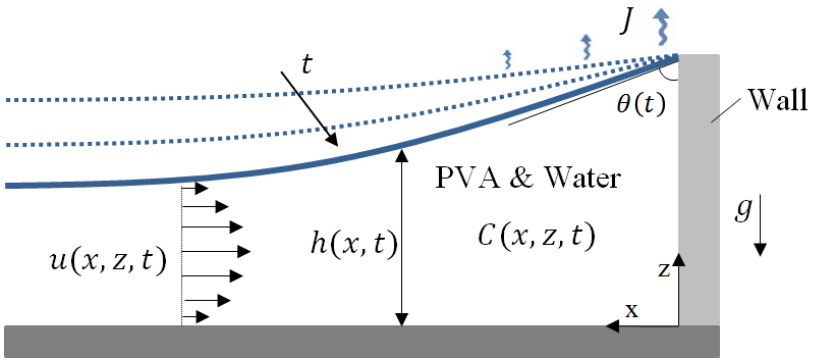

Figure 2-2 Schematic of the physical problem of an evaporating polymer solution inside a cavity next to a vertical wall showing the gravity (g) and the time-varying contact angle.

For the evaporating liquid film, the solvent mass conservation is governed by [31]

$$\frac{\partial h}{\partial t} + \nabla \cdot Q = \frac{J}{\rho} \tag{2.1}$$

where h is the height of the film, J is the evaporation mass flux of the solvent per unit area, ρ is the density, and Q represents the evaporation induced flow rate inside the film per unit width. The flow field ($\mathrm{U} = u\hat{\imath} + w\hat{k}$) is governed by the Cauchy momentum equation. For polymeric solutions, viscosity, density and the surface tension are functions of the polymer concentration (C) that is governed by [31]

$$\frac{\partial}{\partial t}(Ch) + \nabla \cdot CQ = \nabla \cdot (Dh\nabla C) \tag{2.2}$$

where D is the polymer diffusion coefficient in the solution. This means that the mass conservation, momentum and the transport equations are highly coupled and should be solved simultaneously. This could be achieved through a multi-phase numerical simulation that takes into account the changing flow domain, the time varying evaporation rate, as well as the viscosity, surface tension and density change with time and position. Instead, we are taking an experimental approach to investigate this flow problem; our experimental approach is based on our methodology to measure the two-dimensional evaporation-induced velocity field in the x-z plane inside a cavity.

2.3 Experimental methods

2.3.1 Fabrication of the cavity

The cavity in which the fluid evaporation will be studied is made using standard microfabrication techniques. Performing photolithography using the negative photoresist SU-8, a number of square 7 mm × 7 mm cavities are made on a 4 inch Pyrex wafer (Fig. 2-3(a)). The wafer is then cut by a dicing saw and each cavity (Fig. 2-3(b)) is used separately for a different experiment. In order to study the geometrical effects, cavities with different heights ranging from 300 to 800 μm are made with this technique. The transparent Pyrex bottom walls of the cavities allow observing seed particles in the solution inside the cavity with an inverted microscope.

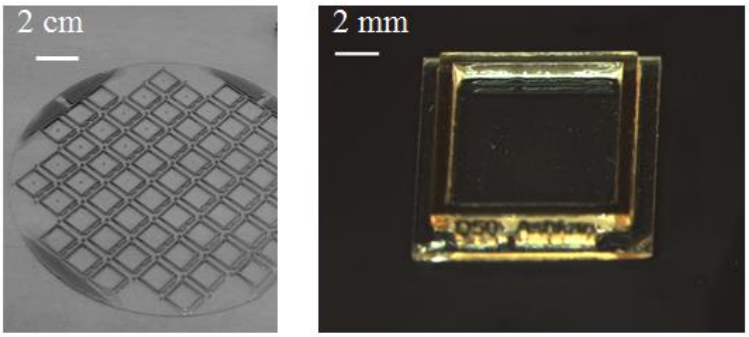

Figure 2-3 (a) Microliter cavities fabricated on a 4 inch Pyrex wafer, (b) one single cavity separated from the wafer.

2.3.2 Solution preparation and characterization

The viscosity of aqueous PVA solutions depends on the molecular weight of the polymer, its degree of hydrolysis, the polymer concentration, and temperature [15]. Solutions of different concentrations of the same low molecular weight PVA (MW~6000 g/mol and 80 % hydrolyzed, Polysciences Inc.) were prepared with deionized water using a revolver mixer at low speed ($\Omega = 5$ rpm) until a uniform and clear solution was achieved. The viscosity of the polymer solutions was measured using a Physica MCR rheometer (Anton Paar) with a bi-cone geometry with a cone angle of 0.983° and a diameter of 59.975 mm. Fig. 2-4 shows the measured viscosity of the aqueous PVA solutions at $T = 25$ ℃ as a function of mass concentration suggesting an exponential relationship of viscosity

$$\mu = 0.0014e^{0.2336 \cdot C/wt\%}\ Pa \cdot s \tag{2.3}$$

as a function of PVA concentration C in wt%. At concentrations above 35 wt%, the solutions become highly viscous with a preparation time of several weeks. Consequently, 35 wt% was selected as the maximum concentration for the rheometry measurements. As expected for dilute PVA solutions [16], no significant shear-thinning behavior was observed in this concentration range. Aqueous PVA solutions can also have viscoelastic properties [15]; however, considering the typical relaxation time $\lambda < 1\,\mathrm{s}$ for our solutions [45] and the maximum shear rates as low as $\dot{\gamma} < \sim 0.002\ 1/\mathrm{s}$ in the evaporation-driven flow result in a Weissenberg number $Wi = \lambda\dot{\gamma}$ much smaller than unity so that viscoelastic effects can be neglected.

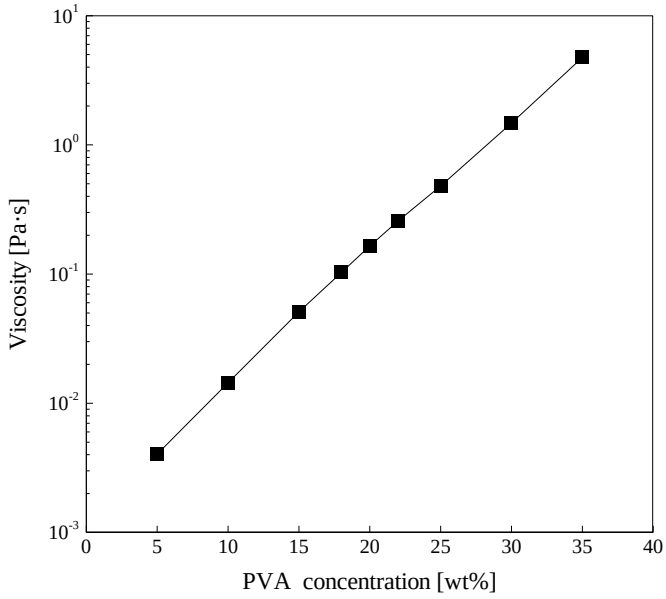

Figure 2-4 Viscosity of aqueous PVA solutions as a function of PVA concentration.

2.3.3 Flow imaging

In order to measure the velocity field of the evaporating fluid next to the vertical wall in the x-z plane as shown in Fig. 2-2, the fluid is seeded with fluorescent particles. As the solution is confined inside the cavity, there is no optical access for the laser sheet and camera set-up used in conventional PIV to image the seed particles. Instead, a combination of confocal microscopy and image processing is used here in order to generate vertical $x - z$ cross-sections of the seed particles in the solution from planar $(x - y)$ images.

For epifluorescence imaging, the solution is seeded with fluorescent particles that are excited with a laser beam and their emission light is captured by a camera through a filter that blocks the excitation wavelength. Here the PVA solution is seeded with $2\ \mu m$ fluorescent polystyrene microspheres (Firefli™ Fluorescent Red (542/612 nm), Thermo-Scientific) to a 0.033% solid concentration of seed particles. A microliter pipette is used to gently fill the cavities with volumes ranging from about $15\ \mu L$ to $40\ \mu L$.. The polymer solutions are all kept in sealed vials to avoid uncontrolled evaporation prior to the beginning of the test. Each cavity is then placed on the microscope stage at a marked position where the scanning is planned. Once the cavity is positioned properly on the stage, it is filled with a polymer solution equal to its volume from the sealed vial and $t = 0$ is defined as the time each cavity is filled and is exposed to controlled evaporation.

The filling of each cavity takes a maximum of $5\,sec$ which defines the uncertainty involved in the definition of $t = 0$. After loading a cavity with the seeded polymer solution, in order to eliminate the environmental effects, it is kept in a temperature controlled microscope stage incubator system at $T = 25 \pm 0.1℃$ for the entire time of an experiment with ambient conditions of $T = 23\,℃$ and relative humidity $RH = 35\%$. Using fluorescent confocal microscopy (Nikon-D-Eclipse C1), a z-stack of planar images is captured by scanning the fluid along the vertical Z axis from top to bottom close to the cavity's wall. A schematic of the scanned volume is shown in Fig. 2-5.

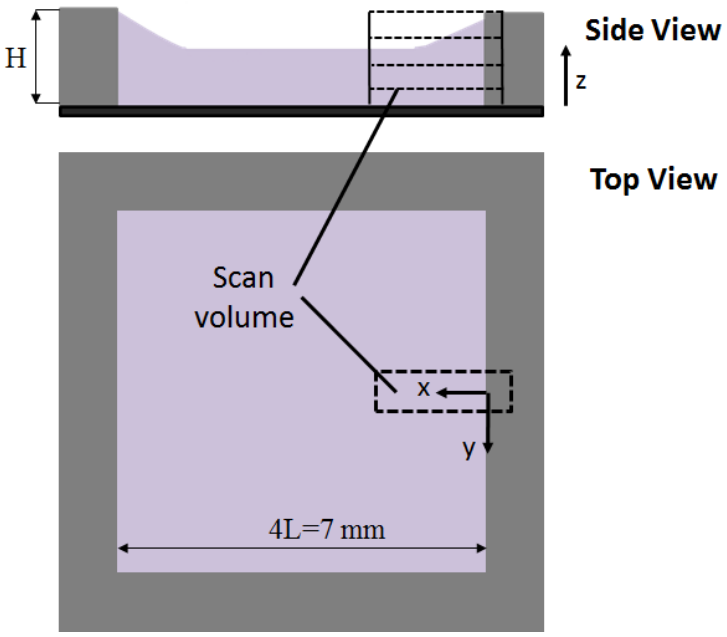

Figure 2-5 A schematic of the cavity with depth H and width 4L showing the scan volume.

A long working distance 10× objective lens with numerical aperture $NA = 0.3$ is used to capture the planar images with a $2.48\ \mu m$ pixel size. The z-direction scanning step size is selected in such a way that the optical slices overlap slightly in order not to lose any data from volume scans. Based on the objective lens, the laser wave length and the confocal pin-hole size, the optical slice thickness (OST) of the confocal system [46] is $22\ \mu m$, and a $13 - 15\ \mu m$ vertical scan step size is used to scan depths ranging from $300\ \mu m$ to $800\ \mu m$. The time required for a full volume scan ranges from $40\ s$ to $70\ s$ depending on the scan depth; volume scans are performed on a continuous basis without delay. The planar images of each volume scan are assembled to generate a 3D image of the fluorescent seed particles by defining a 3-dimensional intensity matrix. A 2D $x - z$ projection image is then constructed from the center of this 3D image by adding the brightness values of 7 adjacent vertical slices for each pixel as shown in Fig. 2-6, and the resulting image is used for PIV analysis.

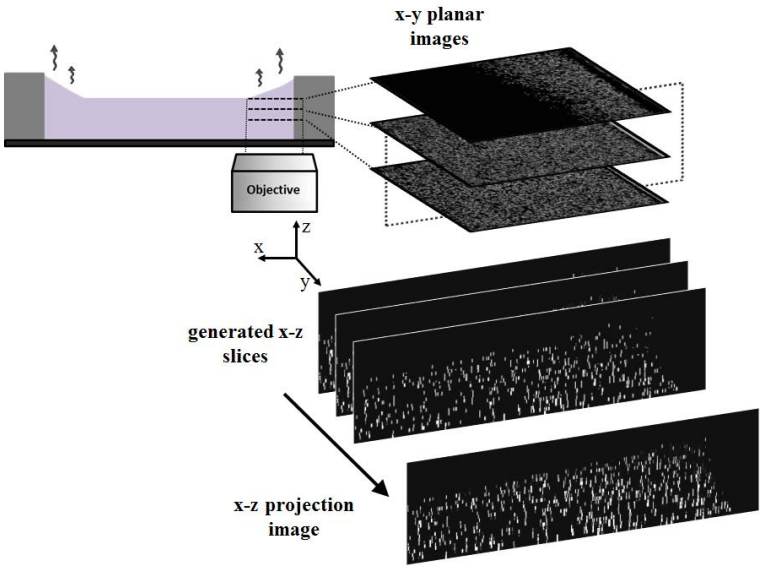

Figure 2-6 The image processing technique used to generate the vertical cross section view from the planar confocal images of the fluorescent seed particles.

2.3.4 PIV analysis

PIV determines the flow field from the displacement of the seed particles. The particle displacement is measured by cross-correlating the fluorescence images of corresponding regions in subsequent images. The velocity vector of each region is then calculated from the displacement vector and the time delay between capturing subsequent images, or here the time required for a volume scan. The time series of the generated $x - z$ images are used to perform a PIV analysis with the software package DAVIS 8.1.5 by LaVision. Multi-pass processing with 22 passes is used for velocity vector calculation. The interrogation window size of 96×96 pixels for the first 11 passes is decreased to 48×48 pixels for the final 11 passes. The overlap percentage is set to 75% in all cases. An elliptical

Gaussian weighting function is used for the interrogation window, because of the dominant horizontal velocity components.

Due to light absorption, the captured emission intensity of fluorescent particles decreases with the increase of distance between the particles and the microscope objective lens. This results in a lower signal to noise ratio and can limit the velocity measurement near the surface; however, using the projection x-z images helps increase the signal to noise ratio to the level required for the PIV analysis. In fact, PIV analysis relies on cross correlation of local emission intensities and does not directly depend on exact emission intensity values.

The measurement of the velocity field in the x-y plane does not reveal any dependence of the velocity field on the y direction. As a result, the two dimensional velocity in the x-z direction is sufficient to describe the flow field.

Due to higher evaporation and lower velocity, the fluorescent particles will have a higher concentration at the surface and their concentration increases toward the contact line. This results in particle aggregation near the contact line which potentiality can influence the evaporation rate. As a result, the initial seed particle concentration is kept very low $(0.03\ wt\%)$ to minimize such effect. In addition, dissolved polymer molecules will also aggregate near the contact line, and it is expected that this effect is more significant since the initial polymer solution is much greater (> 15 wt%) than the particle concentration; consequently, the seed

particle aggregation is not expected to cause any major influence to the flow behavior near the contact line.

2.4 Results and discussions

2.4.1 Velocity field and vortex characterisation

The time dependent velocity field inside an evaporating PVA solution next to a vertical wall is shown in Fig. 2-7 for a 20 wt% PVA solution with initial viscosity $\mu_i = 0.17\ \mathrm{Pa \cdot s}$ in a cavity with a depth of $H = 650\ \mu\mathrm{m}$ and width of $4L = 7\ \mathrm{mm}$; the $x-$and $z-$axis are aligned with the horizontal and the vertical walls, respectively. The principal flow direction is towards the vertical wall. The higher evaporation rate at the pinned contact line at the top of the wall causes a flow towards this region to compensate the excess mass loss. As shown in Fig. 2-7, far from the wall the velocity is mostly unidirectional ($u = u(x, z, t), w = 0$) with a no slip boundary condition at $z = 0$. The velocity at the free surface is affected by the Marangoni flow due to a non-uniform PVA concentration along this surface resulting in near zero velocities at the surface or flow away from the wall. Later in the process, when the surface concentration reaches the glass transition concentration a skin layer forms that forces the velocity at the free surface to zero [47].

Flow recirculation is observed at the corner formed by the vertical and horizontal walls and it is seen that the vortex size decreases during the evaporation process

until no recirculation is seen. Experiments were repeated several times in order to verify the repeatability of the vortex behavior.

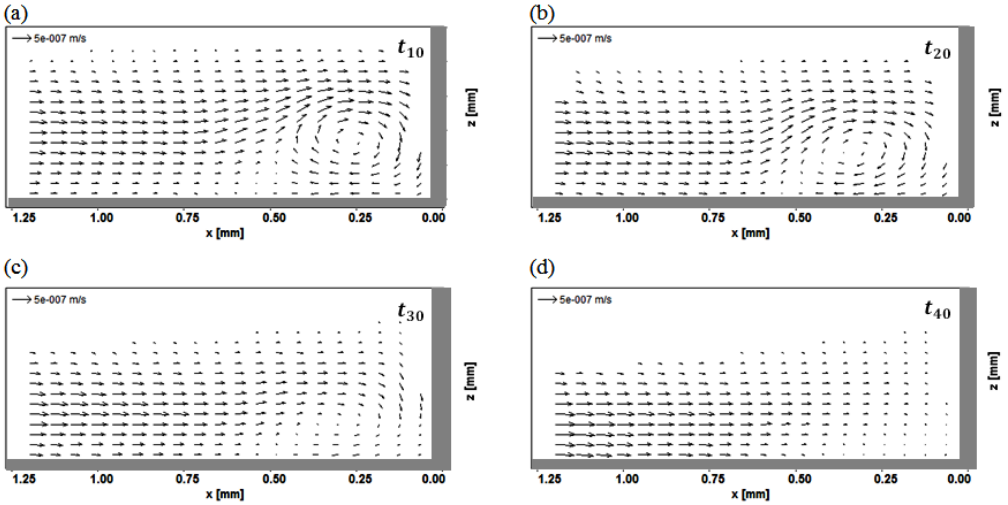

Figure 2-7 Time-dependent velocity field of an evaporating 20 wt% PVA solution in a cavity next to a vertical wall with H=650 µm and width of 4L=7 mm, where $t_i = i\Delta t$ indicates the time passed after the beginning of the evaporation with time delay of $\Delta t = 58\ \mathbf{s}$ between two volume scans

A Reynolds number

$$Re(t) = \frac{\bar{\rho}(t) u_{avg}(t) \bar{h}(t)}{\bar{\mu}(t)} \tag{2.4}$$

can be defined for this problem where u_{avg} is the average evaporation induced velocity towards the wall ($0 < u_{avg} < 1\ \mu\mathrm{m/s}$), $\bar{h}(t)$ is the mean film height and $\bar{\mu}(t)$ and $\bar{\rho}(t)$ are the mean bulk viscosity and mean bulk density of the solution inside the cavity at each time. Both, u_{avg} and $\bar{h}$ are determined at $x = 1.5 \times H$ away from the vertical wall as indicated in Fig. 2-8 since that is the furthest

distance from the vertical wall that could be seen within the field of view of the 10× objective lens for all the cavities. At this point the film thickness $h(x,t)$ is very close to the thickness far from the wall. In order to estimate the average droplet viscosity, it is assumed that the solution height is $\bar{h}$ in the entire cavity and the meniscus near the walls is neglected. This seems to be an acceptable assumption as it leads to less than $\sim 5\%$ error in volume estimation in the most extreme case (late stage of evaporation process). The concentration of the solution inside the cavity is then approximated at each time from $\bar{h}(t)$ and the initial concentration and $\bar{h}(t=0)$. The viscosity is then estimated from the mean PVA concentration of the droplet using the correlation formula (Eq. 2.3) obtained from the rheometry data; the viscosity constantly increases during the evaporation process.

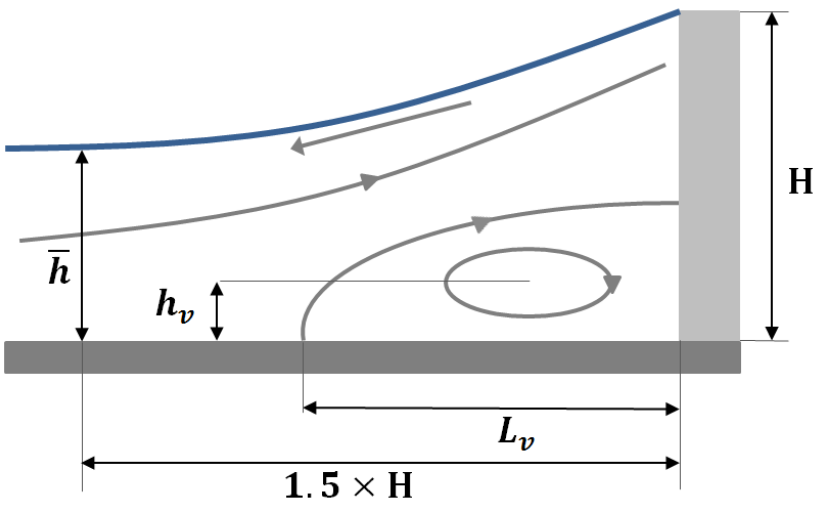

Figure 2-8 Schematic of stream lines and corner vortex characterization.

Eq. 2.4 typically yields a Reynolds number $Re\ (t) < 10^{-5}$ where the viscous forces are dominant and the inertial forces are negligible. As a result, the vortices seen during the evaporation occur in the same low Reynolds number regime as Moffatt vortices.

Similar tests were repeated in different conditions (different ambient temperatures and relative humidity, with and without temperature controlled chamber) and with different procedures (filling at different speeds and using different sizes of micro litter pipettes) in order to make sure that the vortices observed here are not artifacts caused by side effects such as environmental conditions or any filling effects.

2.4.2 Initial viscosity effects

Identical cavities with $H/L = 0.35$ were filled with PVA/water solutions with different initial viscosities in order to further investigate the effect of viscosity on the corner vortex size. The corresponding initial velocity fields are shown in Fig. 2-9 where it is apparent that for the initial viscosity range from $0.1\ \mathrm{Pa \cdot s}$ to $0.26\ \mathrm{Pa \cdot s}$ a higher viscosity leads to a smaller vortex size.

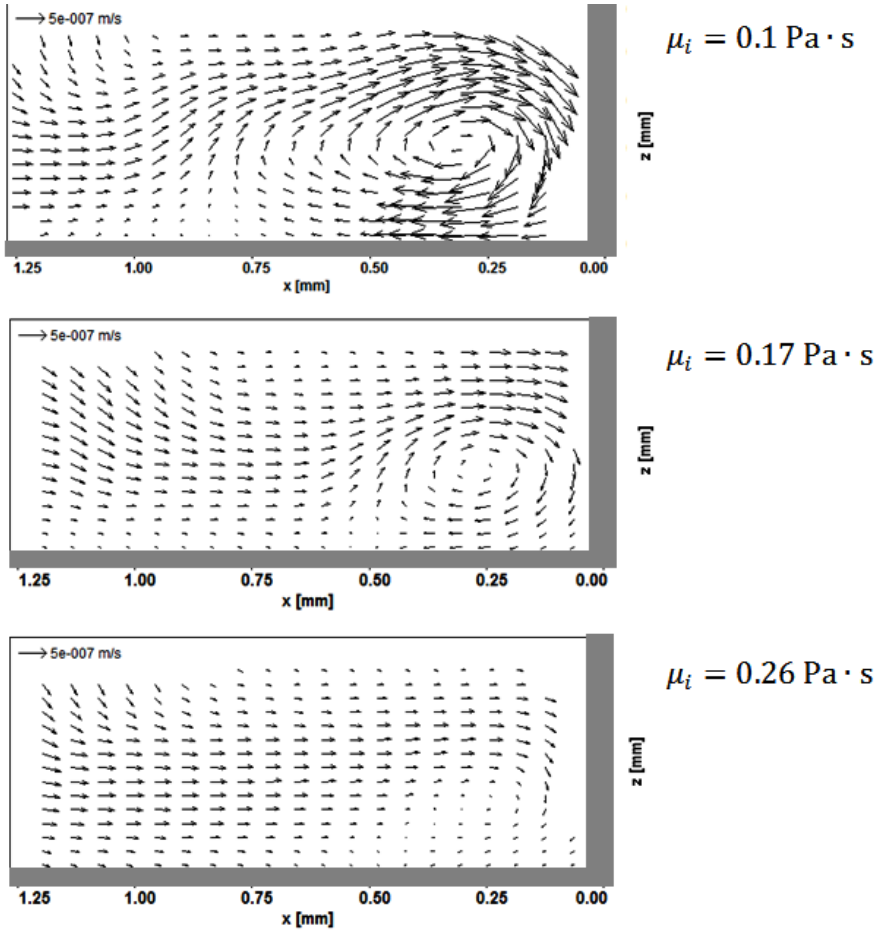

Figure 2-9 Effect of the initial viscosity on the evaporation-induced velocity field in a cavity with $H/L = 0.35$ at $t = 10\ min$ after the beginning of the evaporation process.

The vortex size and position can be characterized with the two parameters h_v and L_v shown in Fig. 2-8. L_v is the distance from the vertical wall where flow separation occurs on the horizontal wall and h_v corresponds to the height of the vortex center. Fig. 2-10 shows these two parameters normalized with the cavity depth. The vortex size and endurance decrease for an increasing initial viscosity. The dimensionless time is defined as

$$t^* = t\dot{\gamma}_{avg}, \tag{2.5}$$

where $\dot{\gamma}_{avg}$ is the time average of the shear rate ($\dot{\gamma}(t) = \frac{u_{avg}(t)}{\bar{h}(t)}$) during the life of the vortex; this shear rate basically stays within a short range ($3 \cdot 10^{-4}\ 1/\mathrm{s} < \dot{\gamma}(t) < \sim 20 \cdot 10^{-4}\ 1/\mathrm{s}$) for all geometries.

The vortex could also be characterized using the vorticity values [48]; however, since the vortex dimensions are used later in chapter 4 to measure the location of the separation point, the vortex size is used for characterizing the vortex. Similar approach has been used in the literature to characterize the vortex in micro geometries using the vortex size [49][50].

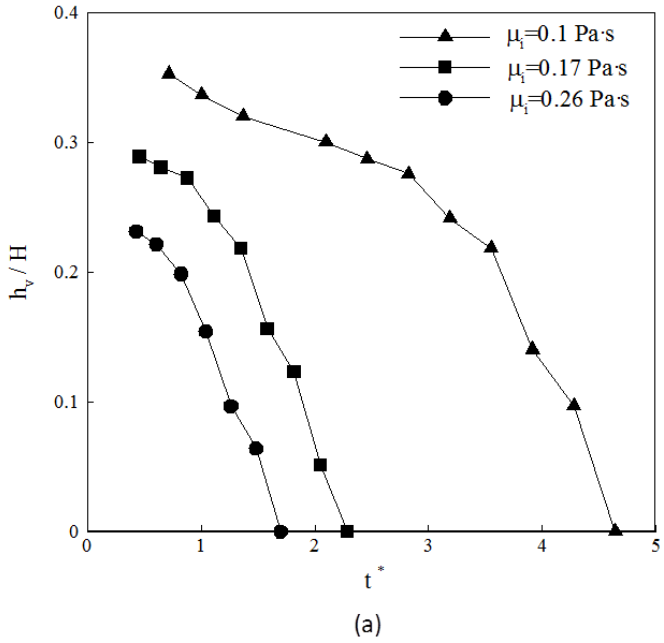

(a)

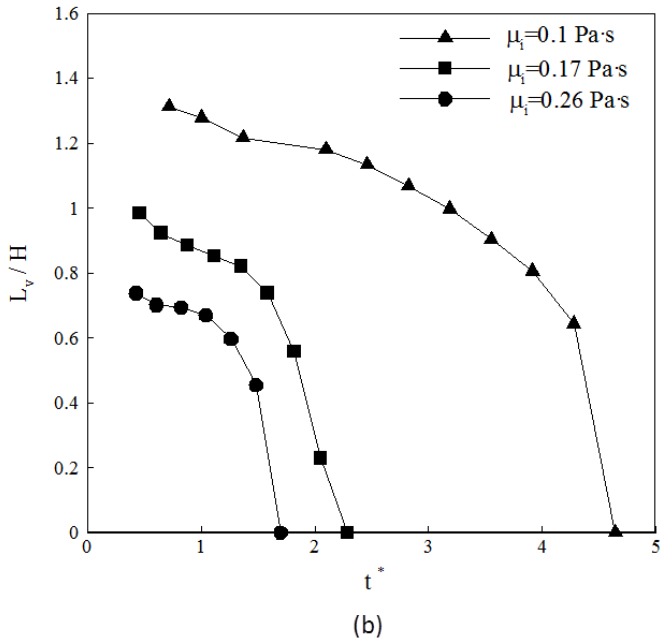

(b)

Figure 2-10 Non-dimensional vortex parameters over time for different initial viscosities in a cavity with $H / L = 0.35$; (a) the vertical position of the vortex center h_v / H, (b) position of the separation point on the horizontal wall L_v / H.

2.4.3 Geometry effects

Similar to other Moffatt vortices the geometry of this flow problem also highly affects the size and endurance of this corner vortex [38][42][41]. In order to investigate the effect of geometry on the vortex size, cavities with 4 different heights ranging from $H/L = 0.25$ to $H/L = 0.44$ are filled with a same PVA/water solution with $\mu_i = 0.17$ Pa · s and the behavior of the corner vortices is studied over time. The initial velocity fields in Fig. 2-11 show that in general the vortex size is smaller for smaller cavity heights, which is consistent with previous studies [42] [41].

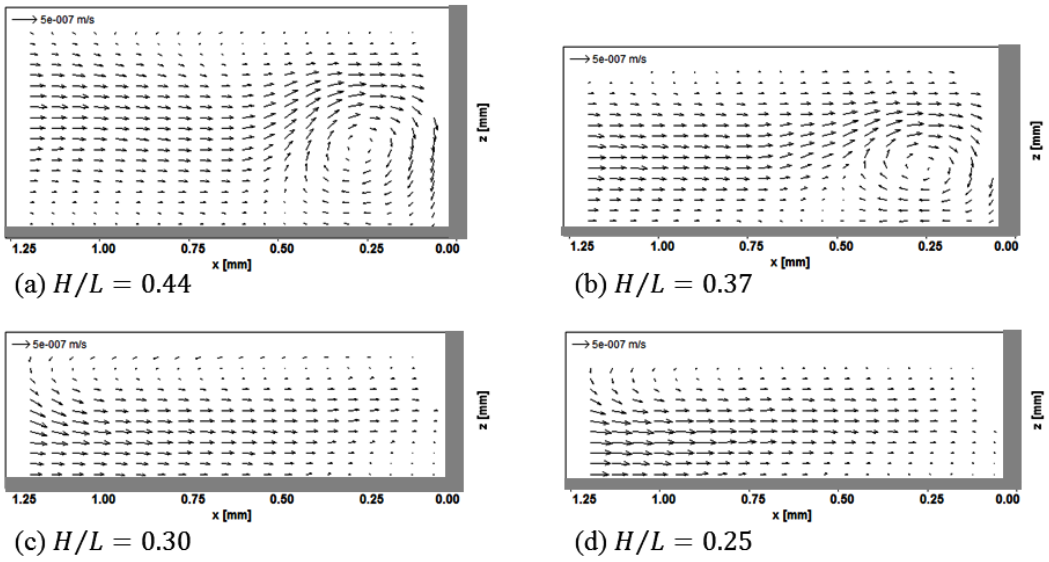

(a) $H/L = 0.44$ (b) $H/L = 0.37$

(c) $H/L = 0.30$ (d) $H/L = 0.25$

Figure 2-11 Velocity fields in cavities with different heights and $\mu_i = 0.17$ Pa · s at t=10 min after the beginning of evaporation.

Fig. 2-12 shows the vortex parameters h_v and L_v normalized with the mean film height ($\bar{h}(t)$) for different cavity depths. It can be observed that the depth of the

cavity highly affects the endurance, size and even presence of the corner vortices. The vortex size and its endurance decrease for smaller wall heights, and for cavities with $H/L < 0.25$ no vortex is observed. Initially, the relative vertical position of the vortex center $h_v/\bar{h}$ stays almost constant before it gradually drops to zero (Fig. 2-12(a)), because both $\bar{h}$ and h_v initially decrease with time at a similar rate. The initial increase of $L_v/\bar{h}$ in time results from an initially constant position of the separation point L_v while $\bar{h}$ is decreasing with time; later, $L_v/\bar{h}$ gradually falls to zero.

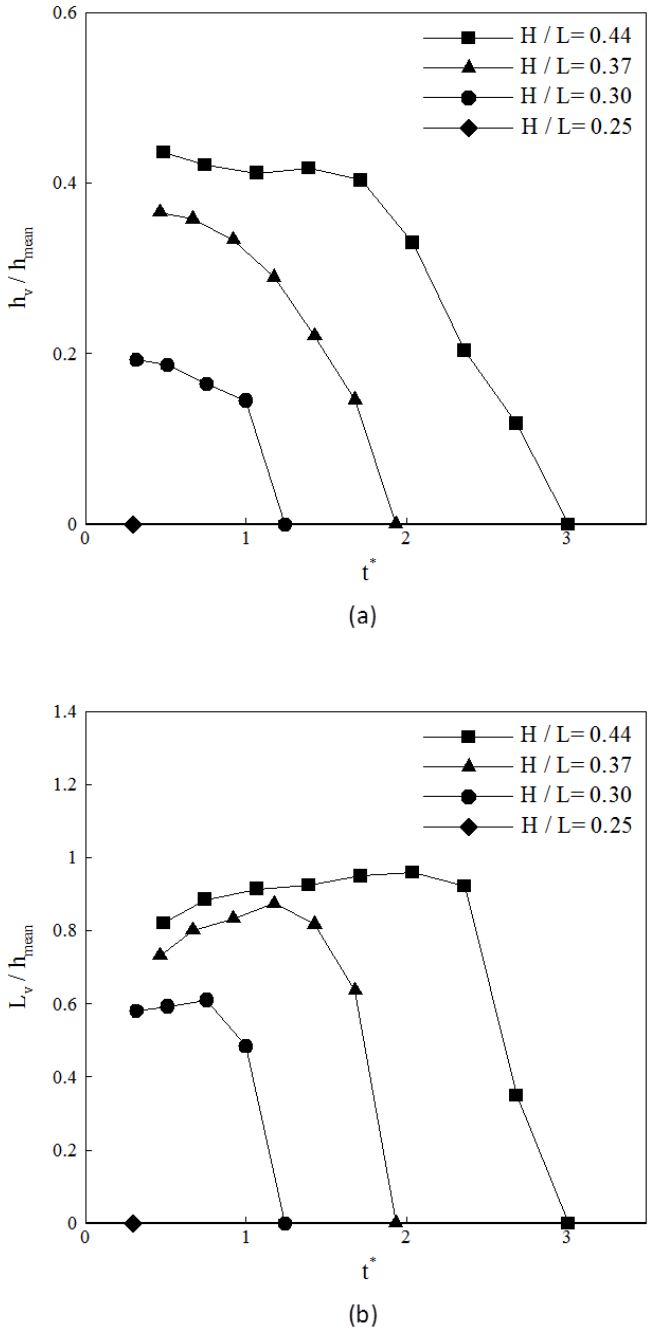

Figure 2-12 Non-dimensional vortex parameters over time: (a) vertical position of the vortex center $h_v/\bar{h}$,, (b) position of the separation point on the horizontal wall $L_v/\bar{h}$.

The vortex size as a function of bulk shear stress ratio is shown in Fig. 2-13. The vortex size decreases at increasing shear stress as before; however, the critical shear stress ratio at which the vortex disappears depends on the cavity depth. For cavities with a higher wall the vortex can persist even until shear stresses as large as $\tau/\tau_{i_{cr}} \cong 10{,}000$; however, no vortex is observed in cavities with a wall smaller than $H = 300\ \mu m$ even for a much lower shear stress. The measurements show that the shear rate slowly increases during the life of the vortex, and it stays within a small range of $3 \cdot 10^{-4}\ 1/\mathrm{s} < \dot{\gamma}(t) < 20 \cdot 10^{-4}\ 1/\mathrm{s}$ for all four cavities. The dramatic increase in shear stress is mostly due to the bulk viscosity increase over time.

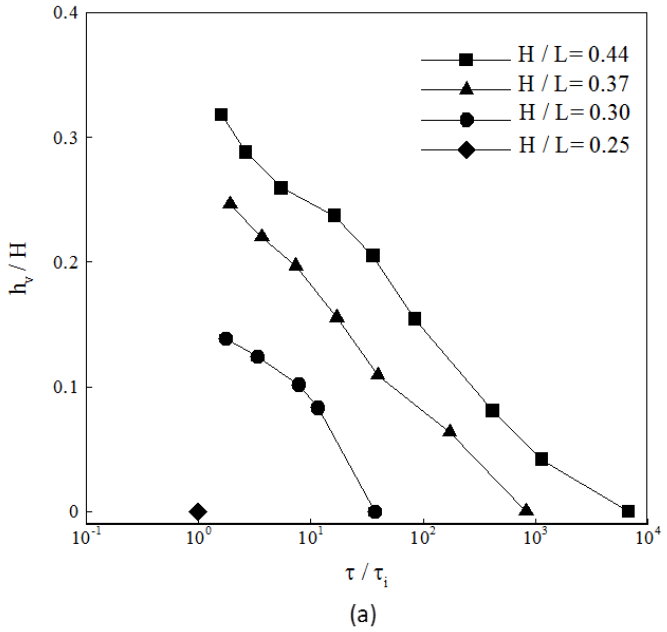

(a)

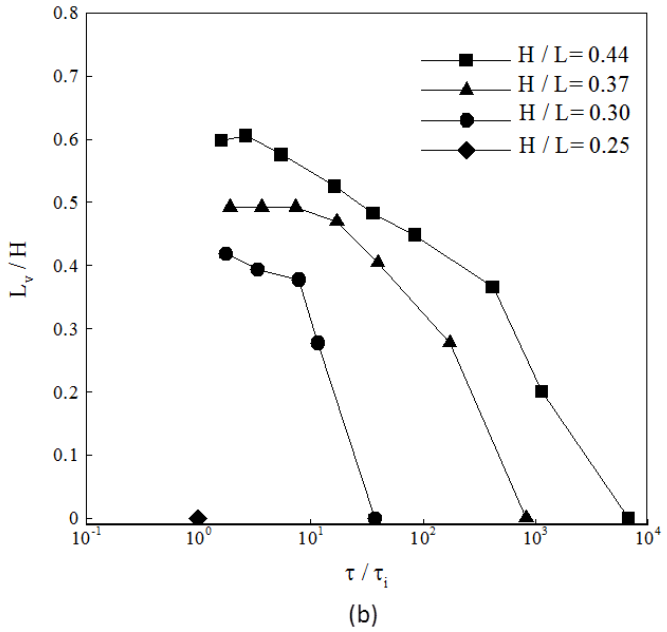

(b)

Figure 2-13 The non-dimensional vortex parameters as a function of characteristic shear stress ratio for different cavity depths (a) the normalized vortex center h_v/H, (b) the normalized vortex length L_v/H.

The dependence of the vortex behavior on the wall height may be explained by referring to the initial velocity fields shown in Fig. 2-11. The top part of each velocity field above the vortex is similar for each height. This part of the velocity field is governed by effects related to the surface, including evaporation and surface tension driven flows. If the vortex only has room at approximately the same distance from the surface, and that region becomes smaller for smaller wall heights, the vortex gets closer and closer to the cavity walls. As a result the viscous friction near the wall is increased, slowing down the vortex. At the same time, the shear stress caused by the evaporation-driven flow promotes vortex rotation. If the vortex rotates much slower than the free stream is pushing it, there will be substantial viscous dissipation in the vortex region, causing the vortex to vanish earlier, at lower shear stress.

For cavities with a depth larger than $H/L \geq 0.44$ multiple vortices can be observed. The velocity field over time of an evaporating PVA/water solution with $\mu_i = 0.17\ \mathrm{Pa \cdot s}$ inside a cavity with $H/L = 0.46$ is shown in Fig. 2-14. During the initial stage of evaporation, only a single corner vortex exists; however, soon, another vortex forms near the free surface rotating in the opposite direction compared to the corner vortex. Finally, a third vortex emerges behind the free surface vortex close to the bottom wall rotating in the same direction as the corner vortex. As the solvent evaporates and the viscosity of the solution increases, the increased shear stress exerted by the flow onto the vortices dissipates them in

reverse order. Evidence of multiple vortices was also seen in the cavity with $H/L = 0.44$ while only the persistent corner vortex behavior over time was reported in Figs. 2-12 and 2-13 for comparison with the time behavior of the single vortices seen in the cavities with $H/L \leq 0.37$. A microscope objective with a larger field of view and lower magnification ($5\times$) was used to investigate the maximum number of vortices that could be observed. Repeated experiments in cavities with $H/L \geq 0.44$ revealed no more than three vortices, although differences were observed in the spacing between the vortices.

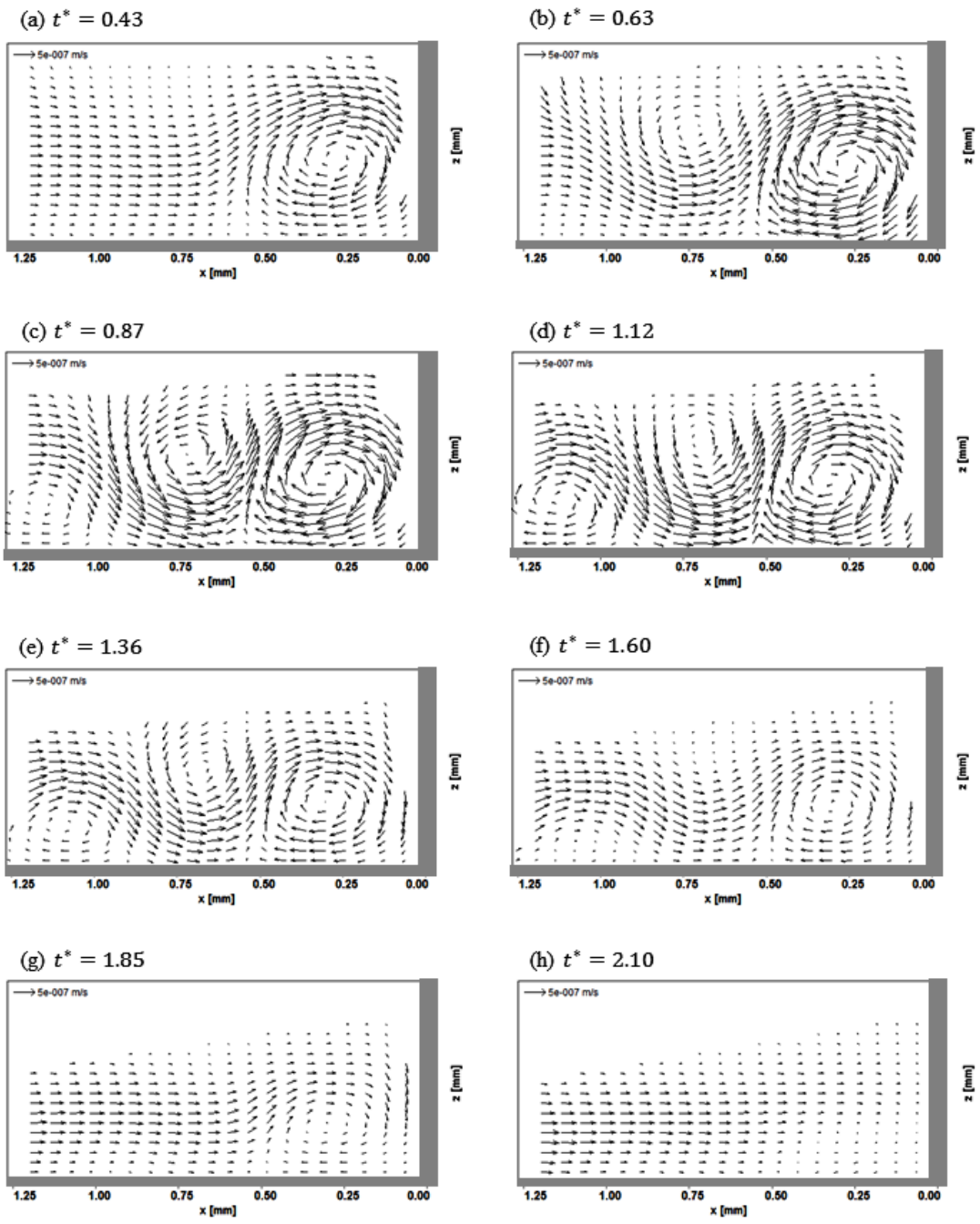

Figure 2-14 Multiple vortices generated during the evaporation of a polymer solution ($\mu_i = 0.17$ Pa · s) inside a cavity with $H/L = 0.46$.

The limited existence of viscous vortices above a critical geometry dimension has also been seen in other studies with different flow-generation mechanisms [51][44].

2.5 Conclusions

We have presented an experimental study to introduce and characterize the low Reynolds corner vortices that can occur during the evaporation of thin films inside microliter cavities. The observed corner vortices all show a similar unsteady behavior, in that they continuously shrink over time and finally disappear. As the bulk viscosity around the vortex is increasing over time, an excess shear stress dampens the vortex. The presence, size and endurance of the corner vortex are highly affected by the geometry, in particular the depth of the cavity. No corner vortex was observed in cavities with a depth smaller than $H/L \leq 0.25$ for $\mu_i = 0.17\ \mathrm{Pa \cdot s}$ while the same solution evaporating in a cavity with $H/L = 0.46$ showed multiple vortices.

These vortices exist at Reynolds numbers as low as $\mathrm{Re}\,(t) < 10^{-5}$ indicating the absence of inertia forces; they are therefore driven by the viscous flow. However, high shear stresses caused by increasing bulk viscosity finally shear these vortices apart. Viscous flow therefore plays a curious role in this flow problem where it is necessary to generate these vortices, while it also makes them disappear.

3 Concentration field evolution near the meniscus

3.1 Introduction

In the absence of full field concentration measurement techniques, the drying of polymer solution films near the meniscus is still not very well understood. Phenomena such as skin formation, which are known from point concentration measurement on flat thin films, are expected to occur at the meniscus as well; however, the concentration values and their variations across the film and during the drying process are not known. In this chapter, a measurement technique is proposed for a full field concentration measurement during the drying of a polymer solution film. Our measurement technique is based on using laser induced fluorescence (LIF) confocal microscopy. The measurement results are compared with the theory and also the velocity field data [52].

3.2 Experimental method

3.2.1 Sample and set-up preparation

Aqueous solutions of a low molecular weight PVA ($MW = \sim 6{,}000\ g/mol$ and 80% hydrolyzed, Polysciences) are made in different concentrations at room temperature using a revolver mixer at a low speed ($\sim 5rpm$).

Microliter sized cavities are fabricated inside a cleanroom using photo-lithography. These cavities are made on a transparent Pyrex substrate in order to allow optical imaging with an inverted microscope. The cavities all have a square base area of $7mm \times 7mm$ with a depth ranging from $H = 300\ \mu m$ to $H = 800\ \mu m$. For each experiment, one cavity is fully filled with an aqueous PVA solution. The filled cavity is then imaged using a 3D laser scanning confocal microscope (Nikon, D-Eclipse C1) while the solvent evaporates from the solution. During the imaging process, the cavity is kept inside a microscope stage incubation chamber (live cell instrument, CU-109) in order to maintain a constant temperature $T = 25 \pm 0.1$ ℃ and to avoid environmental disturbances.

A fluorescent dye (Rhodamine B, Sigma Aldrich ($554/627\ nm$)) is added ($\sim 0.0005\ wt\%$) to the polymer solution for epifluorescence imaging. The laser scanning confocal microscope then scans the solution along the $z-$ axis, from top to bottom, and produces a stack of planar $x-y$ images. A long working distance $10\times$ objective lens with $NA = 0.3$ is used which provides a field of view of

$512 \times 512\ pixels$ with a lateral resolution of $2.48\ \mu m$. In addition, the axial (z −axis) resolution for each image is $\sim 22\ \mu m$ based on the laser wave length, objective lens specifications, and the microscope pin-hole size [46]. The scanning speed is $1 fps$ and $5\ \mu m$ vertical step sizes are used for scanning in the z-direction.

The stack of full-field planar images is then processed to re-construct a 3D image of the solution using a code developed in MATLAB. A projected side view ($x - z$) is then extracted from this 3D image for the measurement of the film profile and for the laser induced fluorescence analysis. A schematic of the experimental set-up is shown in Fig. 3-1.

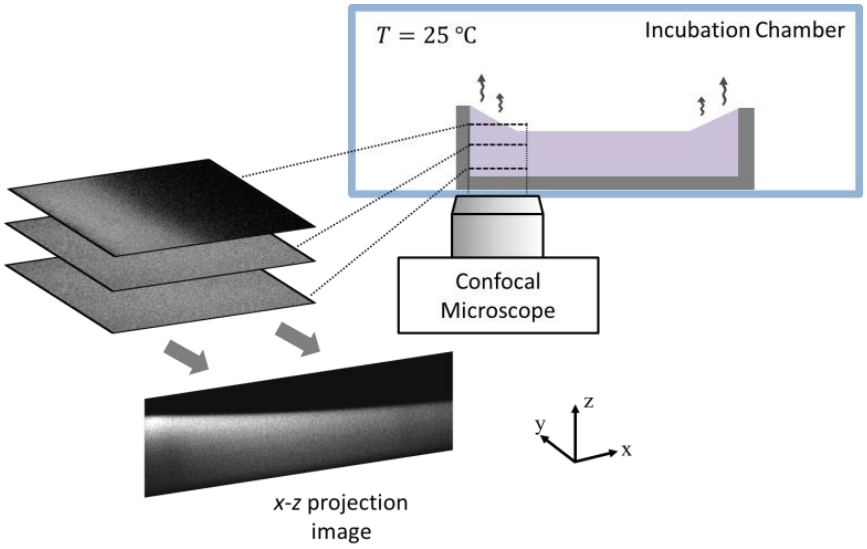

Figure 3-1 The schematic showing the experimental set-up and the imaging technique.

3.2.2 Laser Induced fluorescence analysis

LIF is used to measure the polymer concentration from the $x-z$ projection images. This technique takes advantage of the fact that for dilute solutions the emission intensity of a fluorescent dye captured by an optical scanner,

$$I = AI_i C\varepsilon\phi \tag{3.1}$$

is a linear function of the dye concentration C [53], where A is the collection optics efficiency, I_i is the local incident laser intensity, ε is the dye's absorption coefficient and ϕ is the photoluminescence quantum efficiency of the dye.

For a stable optical set-up, all the parameters in Eq. (3.1) are expected to remain unchanged and the dye concentration field

$$C(x,z,t) = \frac{I(x,z,t)}{I_0(x,z)}\, C_0(x,z) \tag{3.2}$$

can simply be calculated over time where C_0 is the known or initial concentration field of the dye, and I_0 and I are the emission intensity field of the image with the known and unknown concentration field respectively, captured by the confocal scanner.

The linear relationship between the emission intensity and the dye concentration is only valid for dilute solutions. At higher dye concentrations, due to light absorption by the dye, this linear relationship will no longer be valid [54]. As a result, it is important to find the concentration range for which the linear

relationship between the fluorescent emission intensity and the dye concentration is maintained.

In order to find the concentration range for the linear behavior, a wide range of Rhodamine B concentrations ($0.0001\ wt\% - 0.01\ wt\%$) in a PVA solution were 3D imaged inside a covered cavity (no evaporation) using our optical set-up. At very low dye concentrations ($C < 0.0001\ wt\%$) the emission intensity became too scarce to be captured by the confocal scanner. While a linear relationship between concentration and intensity was observed for a wide range of concentrations, at higher concentrations ($C > 0.005\ wt\%$) a significant intensity reduction was observed towards the top of the film due to light absorption.

Considering that the dye concentration increases between 3 to 6 times (depending on the initial polymer concentration) during the experiment, the initial dye concentration was selected in a range ($0.0002\ wt\% < C_0 < 0.0005\ wt\%$) such that the linear relationship between the concentration and the mean intensity across the film is ensured during the experiment.

During the calibration tests (no evaporation), with selected values for C_0, less than 5% intensity reduction observed towards the top of the film for the deepest cavity ($H = 800\ \mu m$) with a constant film thickness across the film. In a similar calibration test (no evaporation) with an initial concentration $6C_0$ in the same cavity, 15% intensity reduction was observed towards the film surface. This

means that with the maximum dye concentration during the evaporation process ($6C_0$) and with the highest film thickness ($h = 800\,\mu m$) the uncertainty of concentration measurement will be 15%; however, during the evaporation process the film thickness decreases continuously everywhere except at the contact line. As a result, highest uncertainty exists for the surface concentration near the pinned contact line (where the largest film thickness is expected) and the uncertainty to be less ($< 15\%$) anywhere else, as the film thickness decreases with the increasing distance from the wall.

The evaporation process starts with a known uniform concentration C_0 across the film. Continuous scanning of the solution provides the cross sectional images of the film $I_0(x, z)$ and $I(x, z, t)$. Eq. (3.2) can then be used to find the concentration field $C(x, z, t)$ across the film at any time during the drying process.

It should be noted that the LIF technique measures the dye concentration and not directly the polymer concentration; however, it can be shown that the dye and the polymer are transported together in the film. In fact, the species inside the thin-film (dye and polymer) are transported by two mechanisms, by convection and by diffusion (Eq. (2.2)) while the convection occurs at much higher rate for both species. As a result, both polymer and dye are transported together by the evaporation induced convection.

The diffusion coefficient of the dye inside a PVA solution can be calculated using the Stokes-Einstein equation

$$D = \frac{k_B T}{6\pi\mu R}, \tag{3.3}$$

where $k_B = 1.38 \times 10^{-23}\, J \cdot K^{-1}$ is the Boltzmann's constant, T is the solution temperature, μ is the solution viscosity and R is the particle radius. Selecting $T = 298$ K and a viscosity $\mu = 0.17$ Pa · s (for PVA solution with $C = 20$ wt%) and considering a dye's molecular radius as $R = 1$ nm (based on reported diffusion coefficients in water [55]) results in an initial diffusion coefficient of $D = 1.28 \times 10^{-12}\, m^2 \cdot s^{-1}$during the evaporation process.

The diffusion rate can be compared with the convection rate using the Peclet number defined as

$$Pe = \frac{u' H}{D}, \tag{3.4}$$

where u' is the characteristic evaporation-induced velocity that is defined as $u' = H/\tau$ with τ being the evaporation time. Assuming $\tau = 60\, min$ for a PVA solution evaporating inside a cavity with $H = 500\, \mu m$ results in $u' = 1.38 \times 10^{-7}\, m/s$ which is also consistent with the PIV results [52]. Using all these parameters results in $Pe_{dye} > 50$ which reveals a negligible initial diffusion rate for the dye inside the solution. In fact, the diffusion rate decreases further as the viscosity

increases during the evaporation process while the evaporation-induced velocity is maintained nearly constant for a long time. A lower diffusion rate is expected for the PVA inside the solution compared to the dye because of the larger size of the PVA molecules. As a result, diffusion plays a negligible role and dye and polymer are transported together mainly by convection. Assuming the radius of water molecule to be $1.5\,\text{Å}$, the diffusion rate is ~ 6 times larger for water molecules inside the solution compared to the dye resulting in an initial $Pe_{H_2O} > \sim 8$. This means that while water molecules are mainly transported by convection, diffusion is also significant, especially at the low initial viscosity.

3.2.2.1 Limitations.

This method has limitations for concentration measurements very close to the vertical wall ($x < 0.2\ mm$), due to shadow effects affecting the intensity field. In addition, near the end of the evaporation process ($\theta < 45^{\circ}$), an artifact appears at the surface near the contact line. This effect is caused by total internal reflection, as the free surface slope reaches the critical angle of the PVA/air interface. Assuming that the surface concentration near the contact line is very close to 100% near the end of evaporation process, the critical angle $\varphi_{cr} = \arcsin(1/n) \approx 42^{\circ}$ can be derived from the refractive index $n = 1.5$ for solid PVA.

The intensity fields of cross section images of the film captured by the confocal microscope are shown in Fig. 3-2. At the beginning (Fig. 3-2(a)), a low uniform

intensity exists across the film; however, higher and non-uniform intensities can be detected across the film, as the evaporation process continues (Fig. 3-2(b)).

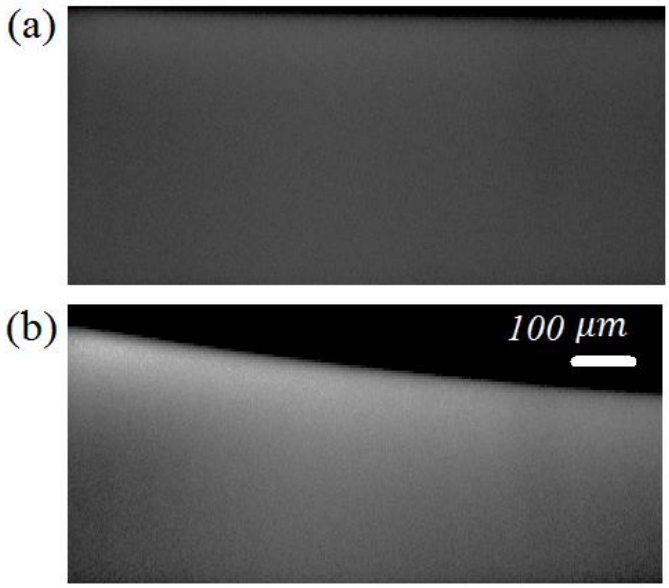

Figure 3-2 The emission intensity fields captured by the confocal microscope, (a) 2 min after the beginning of the evaporation process, (b) 18 min after beginning of the evaporation process

A very close look at Fig. 3-2 reveals a blurry interface at the film surface, caused by the limited axial resolution of the confocal system ($\sim 22\ \mu m$) known also as the optical slice thickness (OST) [46]. This resolution also determines the axial precision for concentration measurement across the film. We define the concentration at the solution-air interface as the highest measured concentration for each position x, and we define the interface as the location where this concentration is found; we estimate an error around $10\ \mu m$ for this method.

3.3 Results and discussion

3.3.1 Contact angle variation

Using the vertical cross section of the film, the contact angle can be measured over time by curve fitting of the surface points with an exponential function as

$$\frac{h\,(x)}{H} = ae^{-b(x/H)} + 1 - a, \tag{3.5}$$

where a and b are time dependent constants to be determined through the fit. This function satisfies the condition that the contact line stays pinned at the top of the vertical wall at $x = 0$ and $z = H$ and becomes flat far away from the wall ($h(x \to \infty) = 1 - a$). The contact angle can be determined from a and b as $\partial h/\partial x(x = 0) = -ab = -\cot\theta$.

Fig. 3-3 shows the contact angle over time for two different sets of experiments. The contact angle over time is representative of the evaporation process.

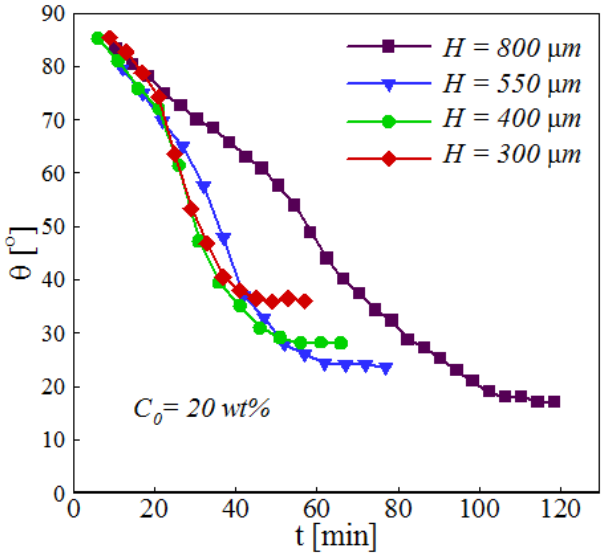

(a)

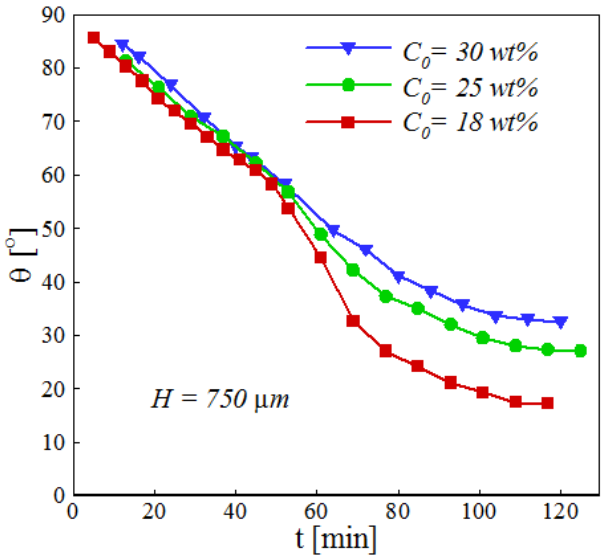

(b)

Figure 3-3 Contact angle over time for an evaporating PVA solution, (a) with $C_0 = 20\ wt\%$ in cavities with different depths, (b) in a cavity with $H = 750\ \mu m$ and different initial concentrations.

Fig. 3-3(a) shows the contact angle versus time for a PVA solution with an initial concentration $C_0 = 20\ wt\%$ evaporating in cavities with different depths. The general behavior is similar in all cases. First the contact angle decreases at a constant rate followed by a short sharp decrease, after which the contact angle decreases slowly again until it approaches a constant final angle. The final angle decreases for increased cavity depths, because the same mass fraction of dried polymer in a deeper cavity results in a smaller final angle. We define the evaporation time τ as the time it takes for the contact angle to become nearly constant (less than 0.5° variation in 10 minutes). The evaporation time increases as the cavity depth increases.

Fig. 3-3(b) shows the contact angle inside a cavity with depth $H = 750\ \mu m$ with three different initial concentrations. The evaporation times are close for all three cases; however, the final angle increases with increasing initial concentration. This is expected as with the same volume of solution, a higher initial concentration results in a larger mass of polymer to be deposited in the cavity which leads to a larger final angle.

A similar trend has been reported for thickness over time of evaporating flat films of PVA solutions. The changing film thickness over time (dh/dt) slows down near the end of the evaporation process [21][22], similar to what is seen here for $d\theta/dt$. This decrease in the evaporation rate has been related to the formation of

a glassy skin layer at the air-solution interface. The skin layer decreases the evaporation rate by limiting the solvent molecule diffusion towards the air-solution interface and prolongs the existence of residual solvent trapped beneath the skin [21][56].

3.3.2 Polymer concentration

Fig. 3-4 shows the concentration field of a PVA solution with an initial concentration $C_0 = 20\, wt\%$ inside a cavity with $H = 550\, \mu m$ over time at different contact angles.

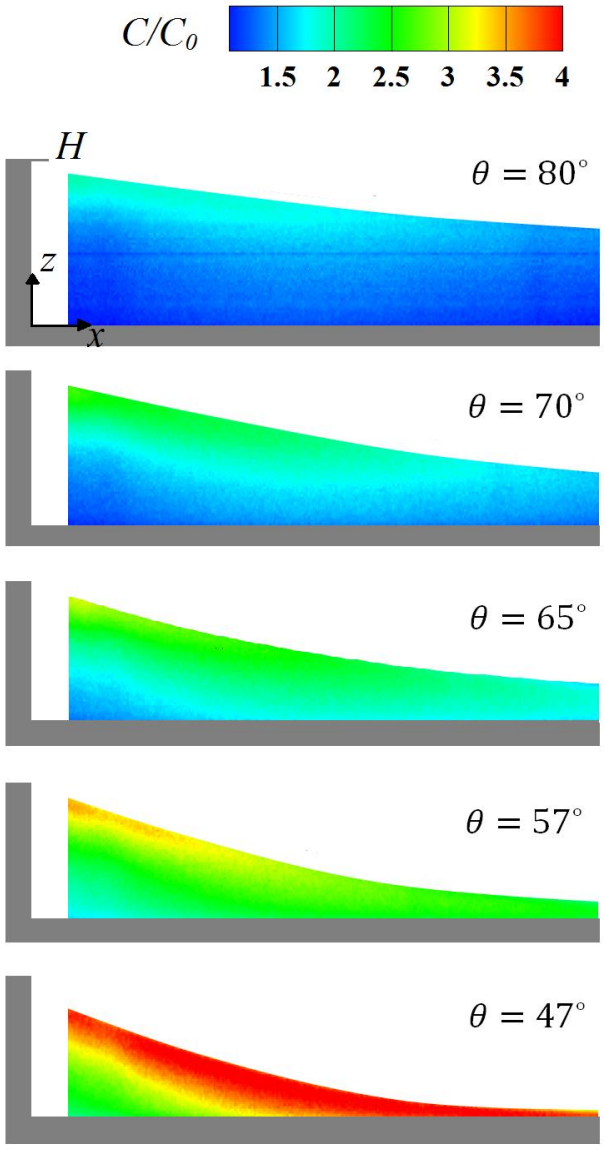

Figure 3-4 Polymer concentration field for an evaporating PVA solution with $H = 550\ \mu m$ and $C_0 = 20\ wt\%$

The concentration at the surface remains higher and increases towards the vertical wall. In fact, the solvent molecules at the surface can evaporate with an increasing rate towards the contact line, due to geometrical effects, resulting in a higher

polymer concentration at the surface; however, the bulk solvent molecules cannot reach the surface due to low diffusion rates [56] and are instead transported with the capillary flow towards the contact line and take the dissolved polymer with them which increases the polymer concentration near the contact line.

Fig. 3-4 shows that significant concentration gradients exist across the film during the evaporation process. For aqueous PVA solutions at room temperature, the solvent induced glass transition occurs at $C_s \approx 80\ wt\%$ [21]. This confirms the formation of a glassy skin layer at $\theta = 47^{\circ}$ where $C_S \approx 80\ wt\%$. The skin layer formation explains the decrease in $d\theta/dt$ shown in Fig. 3-4(a) for $H = 550\ \mu m$ with $\theta < 47^{\circ}$.

From Fig. 3-4, the concentration along the free-surface and the bottom wall are extracted and are shown in Fig. 3-5 for the same contact angles.

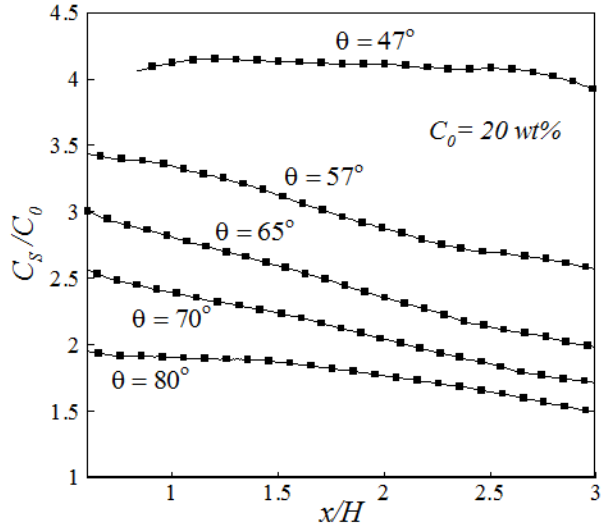

(a)

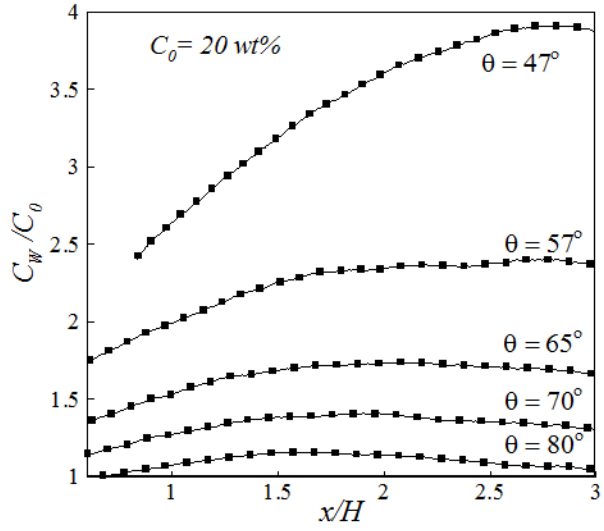

(b)

Figure 3-5 Concentration as a function of distance from the vertical wall with $H = 550\ \mu m$ and $C_0 = 20\ wt\%$, (a) normalized surface concentration, (b) normalized concentration at the bottom wall

Fig. 3-5(a) shows that the surface concentration increases towards the vertical wall ($x = 0$) over time; however, above the glass transition concentration ($C > 80\%$), the concentration gradient decreases at the surface. In fact, after the skin formation the evaporation at the air-solution interface will be very limited and the bulk water molecules slowly reach the skin layer and the surface concentration becomes more uniform. Although diffusion is found to be negligible for dye and polymer, it can still occur for water molecules at a low rate due to their smaller size. The surface concentration profile is of high importance as it affects the Marangoni flow.

Fig. 3-5(b) shows the concentration along the bottom wall for different contact angles. Initially, the concentration gradients are much smaller near the bottom wall compared to the free-surface, and the concentration values stay close to the initial concentration. A significant concentration gradient is observed later at $\theta = 47^{\circ}$ after the skin layer has formed at the surface. The extrapolation of the curve at $\theta = 47^{\circ}$ for $x/H < 1$, reveals a residual solution with high moisture content is trapped at the corner of the cavity.

The effect of the cavity depth on surface concentration for an evaporating PVA solution with an initial concentration $C_0 = 20\, wt\%$ is shown in Fig. 3-6. The surface concentration undergoes a similar evolution regardless of the cavity depth. The concentration and the concentration gradient at the surface increase towards

the vertical wall until around 35% of the evaporation time. At $t/\tau = 0.5$, as the surface concentration goes above the glass transition concentration $C_S/C_0 > 4$, the concentration gradient decreases towards the vertical wall at the surface and becomes nearly constant near $C_S/C_0 = 5$. The concentration at the surface shows a wavy behavior inside the deeper cavity with inflection points around $x/H = 1$ and $x/H = 2$.

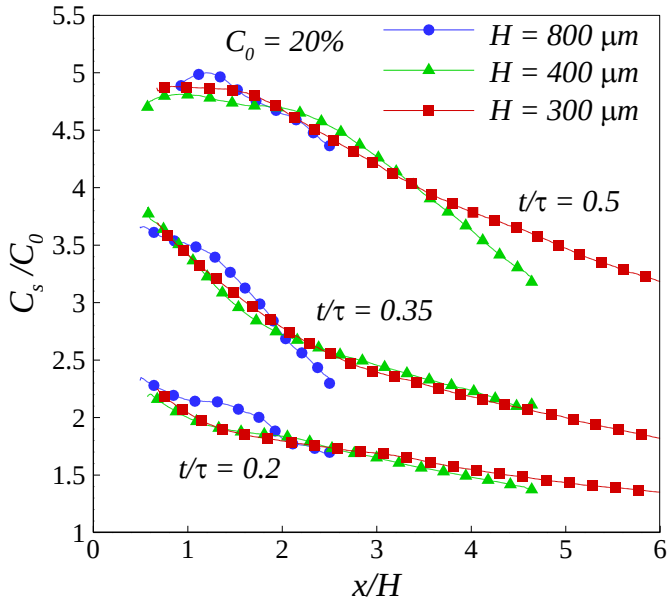

Figure 3-6 Surface concentration over time for an evaporating PVA solution with $C_0 = 20\%$ and different cavity depths

Fig. 3-7 shows the concentration along the free surface for an evaporating PVA solution in a cavity with $H = 550\,\mu m$ at two different initial concentrations. Although some differences are apparent, in general both films have a similar surface concentration. At $t/\tau = 0.3$ with the initial concentration $C_0 = 30\,wt\%$,

the surface concentration becomes almost constant at $x/H < 1$ as the surface concentration gets close to the glass transition concentration ($C_S \approx 80\ wt\%$).

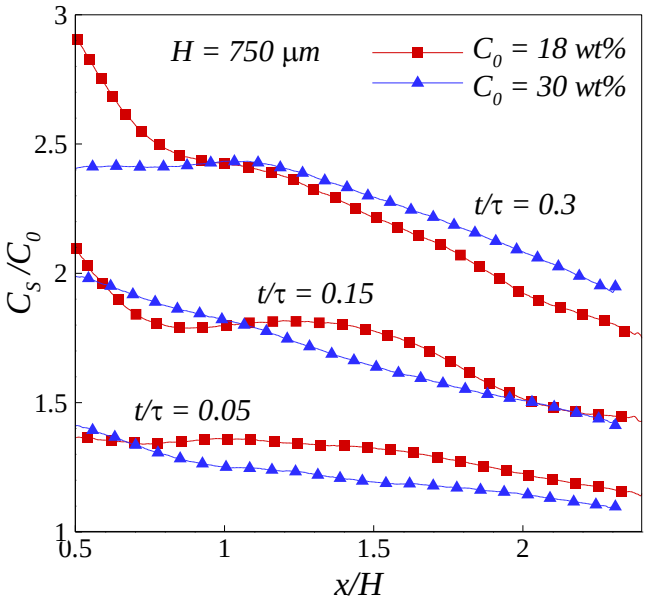

Figure 3-7 Surface concentration over time for evaporating PVA solutions inside a cavity with $H = 550\ \mu m$ with two different initial concentrations

3.3.3 Effect of the Capillary number

The fact that the surface concentration is not significantly affected by cavity depth or the initial concentration as shown in Fig. 3-6 and Fig. 3-7 can be explained based on the theory. Using non-dimensional parameters and neglecting diffusion, Eq. (2.2) can be simplified as

$$\frac{\partial}{\partial t^*}(C^* h^*) + \nabla \cdot C^* Q^* = 0, \tag{3.6}$$

where $C^* = C/C_0$ is the normalized concentration and $t^* = t/\tau$ is the non-dimensional time. $Q^* = \int U^* \cdot dl^*$ is the non-dimensional flow rate with $U^* = U/U_0$ the non-dimensional velocity field and $U_0 = H/\tau$ is the characteristic velocity and $l^* = l/H$ is the dimensionless length.

Eq. (3.6) shows that the normalized polymer concentration C^* is not directly affected by the initial concentration or cavity depth, as these parameters cancel from the equation. In fact, H and C_0 can still influence the concentration field by affecting the velocity field.

Fig. 3-6 and Fig. 3-7 show that the surface concentration has a wavy profile at large H or at small initial concentration. On the other hand, at smaller cavity depths or larger C_0, a more steady profile is observed.

A Capillary number at the surface is defined as [57]

$$Ca = \frac{\mu U_0}{\sigma}, \tag{3.7}$$

where $\mu\,(x, z, t)$, and $\sigma(x, z, t)$ are the local viscosity and surface tension that both depend on polymer concentration, and ρ is mass density of the solution. Using the characteristic evaporation-driven velocity $U_0 = H/\tau$ results in

$$Ca = \frac{\mu H}{\tau \sigma}. \tag{3.8}$$

Fig. 3-8 shows the surface concentration profile for two different Capillary numbers. The Capillary numbers are calculated by assuming a mean surface concentration at $x/H = 2$. This results in $\bar{C} = 1.97 \times 18\ wt\% = 35.5\ wt\%$ and $\bar{C} = 2.02 \times 20\ wt\% = 40.4\ wt\%$ for $H = 750\ \mu m$ and $H = 300\ \mu m$ respectively. The evaporation times for the two cavities (τ) can be estimated from Fig. 3-3. The Capillary number can then be calculated, using the equations for PVA solution viscosity and surface tension as a function of polymer concentration [52] [58].

The higher viscous forces associated with the higher Capillary number dampen the fluctuation caused by the non-uniform surface tension [58] and a more uniform behavior is observed at the surface.

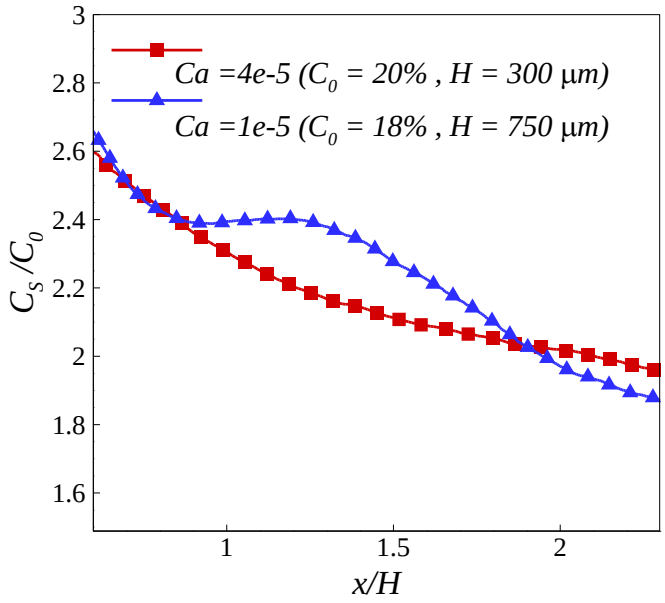

Figure 3-8 Surface concentration at $t^* \approx 0.25$ with two different Capillary numbers

For the two films whose surface concentrations are compared in Fig. 3-8 at $t/\tau = 0.25$, the concentration and velocity fields are provided at a similar time in Fig. 3-9. The velocity fields are measured by micro PIV through a similar imaging process to the LIF analysis, except that the fluorescent dye is replaced with fluorescent seed particles [52].

The velocity field for $Ca = 10^{-5}$ shows that the competition between the capillary pressure and the Marangoni flow results in near zero velocity at the surface and separation points on the bottom wall inside the deeper cavity.

The wavy profile of the surface concentration at $Ca = 10^{-5}$ can be explained in conjunction with the velocity filed. The velocity field shows a significant flow

recirculation near the surface which correlates with an elevated local concentration at the surface between $1 < x^* < 1.5$. At locations where the flow recirculates near the bottom wall, the polymer concentration is locally uniform with a value close to the initial concentration. In fact, the moisture inside the vortex cannot get out except through diffusion which is occurring at a very slow rate. As a result, the local concentration inside the vortex is fairly uniform.

The steady concentration profile at the surface with $Ca = 4 \cdot 10^{-5}$ (Fig. 3-8) is associated with the largely unidirectional velocity field across the film as seen in Fig. 3-9. In fact, it is expected that the local velocity disturbances at the surface are damped here by higher viscous forces. Comparing the Capillary numbers and the surface concentration profiles for different cases reveals that the wavy behavior starts occurring for a capillary number in the range $10^{-5} < Ca < 4 \cdot 10^{-5}$, as the surface tension forces increase compared to local viscous forces.

The higher surface tension associated with a lower capillary number results in local flow recirculation near the free surface which is expected to cause the wavy surface concentration profile. At higher capillary numbers, the higher viscous forces damp local flow recirculations and a more uniform surface concentration profile is observed.

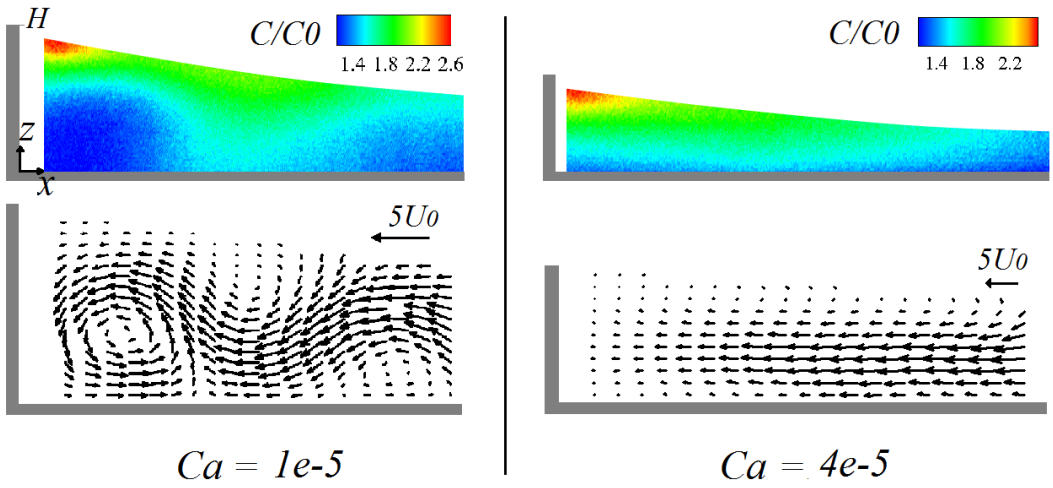

Figure 3-9 Concentration and velocity fields at $t^* \approx 0.25$ for two different capillary numbers

A Marangoni number can also be defined as [58]

$$Ma = \frac{\frac{\partial \sigma}{\partial x} H}{\mu U_0}, \tag{3.9}$$

where σ is the surface tension of PVA solution. Since the viscosity of the PVA solution increases exponentially with the increase of polymer solution [52], the Marangoni number decreases over time and changes along the surface; however, a maximum Marangoni number can be estimated. Assuming a maximum of $0.02\ N/m$ surface tension difference along the surface [58] over the length $2H$, and assuming a minimum initial viscosity of $\mu_i = 0.17\ Pa \cdot s$ with $U_0 = 0.1\ \mu m/s$ results in a maximum $Ma = 5.8 \times 10^5$.

This reveals that at the beginning of the evaporation process, the Marangoni forces are much larger than the viscous forces; however, over time the Marangoni

forces decay as the concentration becomes uniform along the surface and while the viscosity sharply increases due to solvent evaporation.

3.3.4 Effect of flow recirculation on the structural properties of the dried polymer

Inside the vortices near the bottom wall, the local concentration stays very close to the initial concentration while the bulk concentration is increasing and forming a rubbery phase around the vortex. While there is enough time and mobility inside the rubbery phase for polymer crystallization[23], this crystallization process will be postponed inside the vortex until the vortex disappears[52]. In fact, a sufficiently significant polymer interaction is required for crystallization which this is not possible at the low polymer concentration inside the vortex. As a result, it is expected that polymer crystallization inside the corner vortex occurs at a much slower rate during the evaporation and therefore leads to a different microstructure of the deposited PVA in that region [22]. This can affect the mechanical strength of the microstructures (e.g. microneedles) fabricated by the solvent casting process.

3.4 Conclusions

The concentration field was measured during the drying of a thin film of an aqueous PVA solution near a meniscus. The concentration increases in general

over time while concentration heterogeneities exist along the surface and across the film. The concentration at the solution-air interface stays higher than the bulk concentration and increases towards the contact line. The evaporation rate sharply decreases after the surface concentration reaches the glass transition concentration and a skin layer starts forming at the surface. After the skin layer formation, the concentration becomes uniform at the surface, while residual moisture is trapped at the corner of the cavity beneath the skin layer.

Consistent with theory, the normalized surface concentration shows similar behavior as a function of normalized distance from the vertical wall during the drying process, regardless of cavity depth and initial polymer concentration; however, the capillary number is shown to be influencing the surface concentration profile. The viscous forces involved with larger capillary numbers have a damping effect on velocity disturbances at the surface, resulting in a more uniform surface concentration profile. Concentration results are in agreement with PIV results showing a uniform concentration at locations where flow recirculation causes a uniform local concentration.

Results provided in this chapter, help clarify the drying process of polymer solutions near the meniscus. In addition, the described optical measurement technique could help with full-field concentration measurements in a variety of different evaporation studies for colloidal thin-films and droplets.

4 The theory of viscous flow separation

4.1 Introduction

The new recirculation described in Chapter 2 is different from the Marangoni recirculation [30], as it is initiated near the substrate and not at the free surface of the thin film. The fact that the flow recirculation starts on the bottom wall and there is a sign change in the wall shear stress, indicates possible flow separation on the bottom wall during the evaporation process; however, based on the current theory for the flow separation, separation occurs only when a fluid with decreasing inertia has to flow against an increasing adverse pressure gradient. As the flow velocity inside the boundary layer falls to zero, the flow becomes detached from the surface and takes the form of eddies and vortices. This chapter provides a mathematical model based on lubrication theory that describes this flow separation at the creeping flow limit in the absence of inertia during the drying of thin films. The model is validated by experimental data from Chapter 2 and Chapter 3. Viscous flow separation adds to the current understanding of the

flow physics during the drying of thin films, in addition to the well-known evaporation induced capillary transport or the so-called coffee-ring effect and the Marangoni effect.

4.2 Mathematical modelling

A schematic of the flow field along with an experimental velocity field from micro-particle image velocimetry (PIV) is shown in Fig. 4-1.The fluid used here is an aqueous solution of a low molecular weight PVA ($MW = 6{,}000\,\mathrm{g/mol}$, $80\%\,\mathrm{hydrolized}$) with an initial concentration $C_0 = 18\%$. There is a main capillary flow towards the vertical wall. In addition, flow separation occurs at the bottom wall at a distance x_{sep} away from the vertical wall. The gradient of the horizontal flow velocity u in the z direction on the bottom wall becomes zero at x_{sep} and then changes sign. This satisfies the first condition required for flow separation [48]. As mentioned, the conventional inertial flow separation requires the presence of an adverse pressure gradient; however, here we show that flow separation can also occur at the micro-scale in absence of inertia and an adverse pressure gradient, but due to two different competing forces, rather than for conventional flow separation.

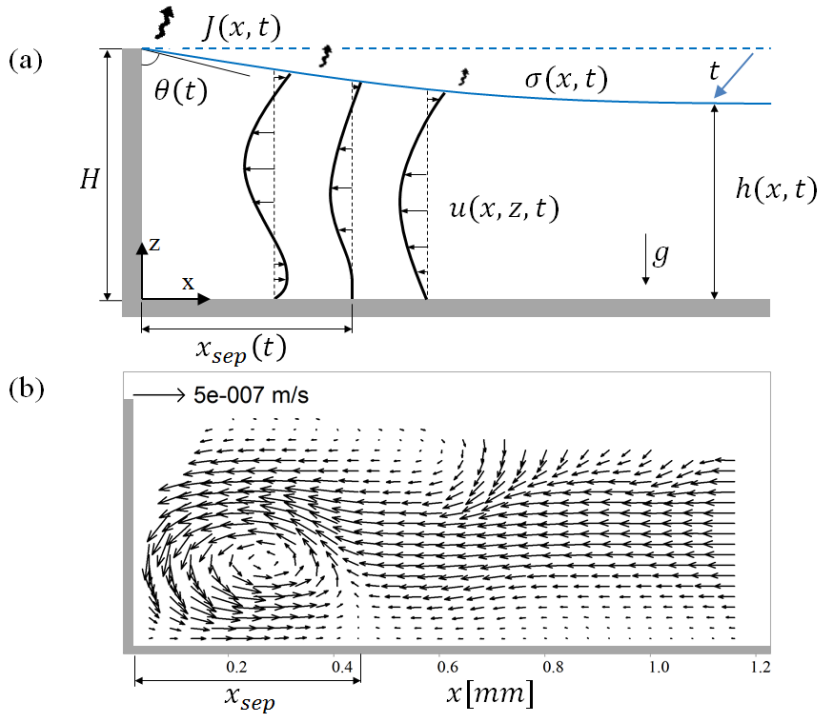

Figure 4-1 (a) Schematic of the flow physics and the horizontal velocity component of the flow field, (b) velocity field inside an evaporating aqueous PVA solution near a vertical wall measured by micro-PIV.

Here $u(x,z,t)$ is the velocity in the x-direction governed by the Navier-Stokes equations which are simplified by the lubrication approximation to [57], [59], [60]

$$-\frac{\partial p}{\partial x}+\frac{\partial}{\partial z}(\mu\frac{\partial u}{\partial z})=0\,, \tag{4.1}$$

where p is the local static pressure and μ is the dynamic viscosity that increases over time for a polymer solution as the solvent evaporates [61]. The lubrication approximation is suitable here because for a Reynolds number $Re=\bar{u}\rho H/\mu<10^{-6}$ [52] with the average flow velocity $\bar{u}$ the inertial forces can be neglected

compared to the viscous forces; in addition, the direction of flow near the bottom wall is mainly unidirectional. The term including viscosity derivative $\frac{\partial \mu}{\partial z}\frac{\partial u}{\partial z}$ in Eq. (4.1) is also neglected, as the viscosity gradient is minimal near the bottom wall where the flow separation occurs; we are interested in evaluating this equation at the bottom wall in order to locate the separation point. In fact, the most significant concentration/viscosity gradient occurs towards the free surface associated with the continuous evaporation. In addition, this assumption does not affect the prediction of the separation point location because the separation point is characterized by $\partial u/\partial z = 0$ which results in $\frac{\partial \mu}{\partial z}\frac{\partial u}{\partial z} = 0$.

The boundary conditions for Eq. (4.1) are the no-slip condition at the bottom wall ($u(z = 0) = 0$) and the Marangoni stress at the free surface $\mu\, \partial u/\partial z\, (z = h) = \partial \sigma/\partial x\, (z = h)$ with the surface tension σ. Solving Eq. (4.1) with these boundary conditions, results in [62]

$$u = \frac{\partial \sigma/\partial x}{\mu} z + \frac{1}{\mu}\frac{\partial p}{\partial x}\left(\frac{z^2}{2} - zh\right). \tag{4.2}$$

The velocity profile in Eq. (4.2) does not apply to locations where significant vertical velocities exist in the film such as near the vertical wall as shown in Fig. 4-1(b), but it is valid near the bottom wall where the flow is 1D and unidirectional parallel to the bottom wall.

The pressure in Eq. (4.2) can be assumed as [63]

$$p = \rho g(h - z) - \sigma \frac{\frac{\partial^2 h}{\partial x^2}}{\left(1 + \left(\frac{\partial h}{\partial x}\right)^2\right)^{1.5}}\ , \tag{4.3}$$

so that under the assumption of a small surface slope $\partial h/\partial x \ll 1$ and consequently with $1 + (\partial h/\partial x)^2 \approx 1$ [62] [32] the pressure gradient becomes

$$\frac{\partial p}{\partial x} = \rho g \frac{\partial h}{\partial x} - \sigma \frac{\partial^3 h}{\partial x^3} - \frac{\partial \sigma}{\partial x}\frac{\partial^2 h}{\partial x^2}. \tag{4.4}$$

Using non-dimensional parameters, the dimensionless pressure gradient can be found as [53]

$$\frac{\partial p^*}{\partial x^*} = \frac{1}{\mathrm{Ca}}\left(\mathrm{Bo}\frac{\partial h^*}{\partial x^*} - \frac{\partial^3 h^*}{\partial x^{*3}} - \mathrm{S}\frac{\partial^2 h^*}{\partial x^{*2}}\right), \tag{4.5}$$

where $p^* = p/p_c$ with the characteristic pressure $p_c = \mu U_0/H$, and U_0 is the characteristic velocity defined as $U_0 = \mu/\rho H$. Also, $x^* = x/H$, $h^* = h/H$, $\mathrm{Ca} = \mu \mathrm{U}_0/\sigma$ is the capillary number, $\mathrm{Bo} = \rho g H^2/\sigma$ is the Bond number, and $\mathrm{S} = (H\partial\sigma/\partial x)/\sigma$ is the non-dimensional surface tension gradient.

Replacing the pressure gradient in Eq. (4.2) and using non-dimensional parameters results in

$$u^* = \frac{\mathrm{S}}{\mathrm{Ca}}\ z^* + \frac{1}{\mathrm{Ca}}\left(\mathrm{Bo}\frac{\partial h^*}{\partial x^*} - \frac{\partial^3 h^*}{\partial x^{*3}} - \mathrm{S}\frac{\partial^2 h^*}{\partial x^{*2}}\right)\ \left(\frac{z^{*2}}{2} - z^* h^*\right), \tag{4.6}$$

where $u^* = u/U_0$ and a Marangoni number can be defined as $\mathrm{Ma} = \mathrm{S}/\mathrm{Ca}$.

The location of the separation and detachment point ($x^*_{sep} = x_{sep}/H$) on the bottom wall can be found from Eq. (4.6) by setting the shear-rate or equally the shear-stress on the bottom wall to zero

$$\mathrm{Ca}\frac{\partial u^*}{\partial z^*}(z^* = 0) = \mathrm{S} + \left(\mathrm{Bo}\frac{\partial h^*}{\partial x^*} - \frac{\partial^3 h^*}{\partial x^{*3}} - \mathrm{S}\frac{\partial^2 h^*}{\partial x^{*2}}\right)(-h^*) = 0. \tag{4.7}$$

Eq. (4.6) and Eq. (4.7) are valid near the bottom wall as the flow is unidirectional parallel to the wall (Fig. 4-1(b)). Eq. (4.7) can be solved to find the location of the separation point on the wall over time if the film thickness h^* and the non-dimensional surface tension gradient S are known as a function of x^* over time.

4.3 Analysis

We are using experimental data for h^* and S to determine the separation length over time using Eq. (4.7), and we then validate this result through comparison with the separation points measured experimentally using micro-PIV (Fig. 4-1(b)).

The fluid has been fluorescently dyed with an initial 0.0005 $wt\%$ of Rhodamine B [52] in order to determine the film profile over time using confocal microscopy. The identified film surface points are curve-fitted with an exponential profile as

$$h^* = ae^{-bx^*} + 1 - a, \tag{4.8}$$

with a and b time dependent constants as shown in Fig. 4-2. This profile satisfies the condition that the contact line stays pinned to the vertical wall over time at

$h^*(x^* = 0) = 1$. Also, at distances far enough from the wall, the surface profile becomes flat as the effect of the wall becomes negligible. The surface slope at $x^* = 0$ can be calculated from Eq. (4.8) and can be related to the contact angle θ as $\partial h^*/\partial x^*(x^* = 0) = -ab = -\cot\theta$. Hence, a in Eq. (4.8) can be replaced with $a = \cot\theta\,/b$.

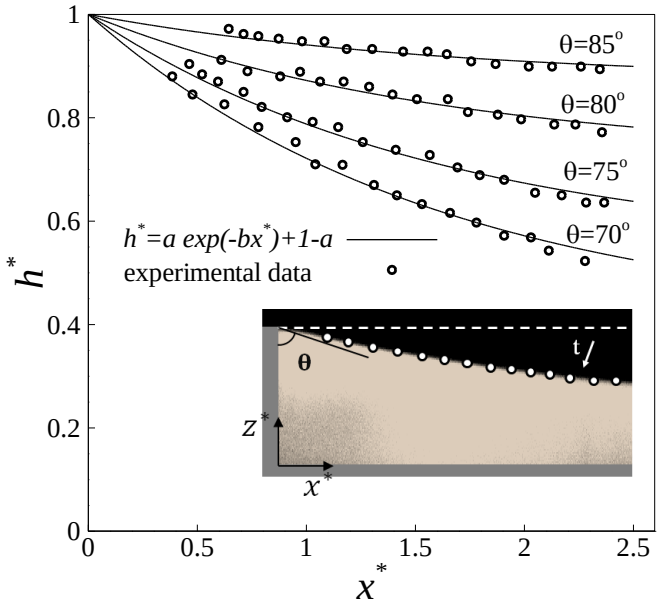

Figure 4-2 Curve-fitting of surface data points with an exponential profile for an evaporating PVA solution with an initial concentration $C_0 = 18\%$ near a vertical wall with $H = 750\ \mu m$; the inset shows a cross section of the PVA solution that is fluorescently dyed with Rhodamine B.

Applying the exponential film profile in Eq. (4.8) to Eq. (4.7) yields the separation point

$$x^*_{sep} = \left(\frac{-1}{b}\right) Ln\left[\frac{\mathrm{S}\, tan(\theta)}{(b^2 - \mathrm{Bo} - \mathrm{S}b)h^*}\right] \tag{4.9}$$

in a compact form; it should be noted that the quantities S and h^* in this equation need to be evaluated locally at x^*_{sep}. As a consequence, Eq. (4.9) needs to be solved iteratively in order to find x^*_{sep}. However, Eq. (4.9) reveals all the important parameters affecting the separation point location. The separation point location is dependent on the non-dimensional surface tension gradient S, the free surface profile including the contact angle and the Bond number.

Considering the measured values of $b = 0.62$, and $\mathrm{Bo} = 0.12$ and a mean value of $\bar{\mathrm{S}} = 0.05$, reveals that the term $\mathrm{S}b$ can be neglected and Eq. (4.9) can be simplified as

$$x^*_{sep} = \left(\frac{-1}{b}\right) Ln\left[\frac{\mathrm{S}\, tan(\theta)}{(b^2 - \mathrm{Bo})h^*}\right] \tag{4.10}$$

The non-dimensional surface tension gradient S is also found using an experimental approach. The addition of the fluorescent dye Rhodamine B to the PVA solution allows using laser induced fluorescence (LIF) to measure the dye concentration over time; as shown in Chapter 3 rhodamine B and the type of PVA used here have different diffusion coefficients inside the solution, but the diffusive time scales for both species are much longer (>50 times longer) than the convective time scales in this flow problem. This means that convection, caused

by the evaporation-driven capillary flow, is the dominant transport mechanism for both the dye and the polymer inside the solution; consequently, the dye concentration is representative of the polymer concentration as they are transported together through convection [52]. The surface tension of low viscosity PVA/water solutions ($C < 20\ wt\%$) was measured at different concentrations using an Attension Theta tensiometer (KSV Instruments). This data and the surface tension for solid PVA ($C = 100\ wt\%$), were fitted to an existing model [8] to yield $\sigma\ (C) = 0.0519 \exp(-0.003C\ /wt\%)\ \mathrm{N/m}$ for PVA/water solutions with $C > 5\ wt\%$. The measured concentration at the film surface over time along with $\sigma\ (C)$ then yield the surface tension $\sigma\ (x, t)$ along the surface over time as well as $\partial\sigma/\partial x$ and S.

The experimental values of S are shown in Fig. 4-3 for different angles during the evaporation process; at the very first moment when the surface profile is flat ($\theta = 90^o$), the evaporation rate away from the wall is nearly uniform yielding $\mathrm{S} = 0$. As the evaporation process progresses and the contact angle decreases, the polymer concentration at the surface increases overall towards the wall resulting in a lower surface tension near the wall and higher positive S values compared with the near-zero S far from the wall; a local S minimum develops around $x^* \approx 1$. This is correlated with a region with a slight increase in polymer concentration beyond $x^* \approx 1$; such non-monotonous S behavior is associated with a

recirculation region near the surface (Fig. 3-9). Finally, as the solution starts solidifying, the concentration gradient decreases along the film surface and S gradually goes to zero again before the end of the evaporation process ($\theta < 50^{\circ}$).

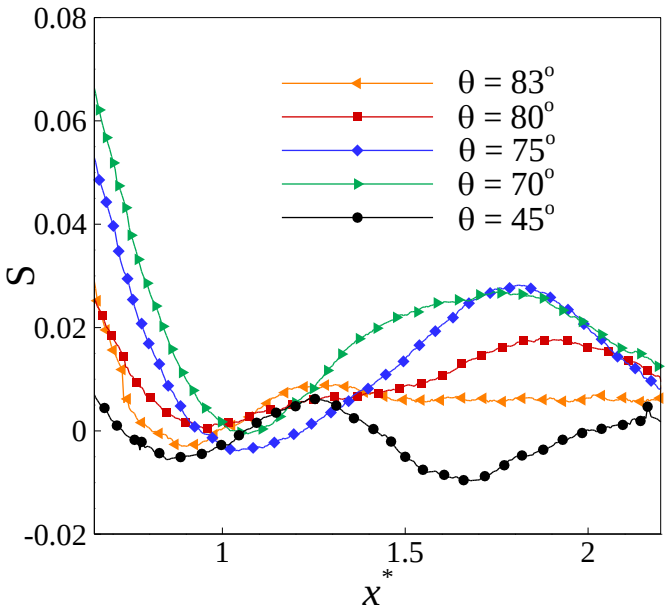

Figure 4-3 Non-dimensional surface tension gradient S as a function of the non-dimensional distance from the vertical wall for different contact angles for a PVA solution with an initial concentration $C_0 = 18\%$ evaporating near a vertical wall with $H = 750\ \mu m$.

Now, that both $h^*(x^*)$ and $S(x^*)$ have been determined over time, Eq. (4.7) or Eq. (4.9) can be used to find the separation point(s) over time, or as a function of the contact angle. Eq. (4.7) includes the two competing forces causing the flow separation on the bottom wall. Here, the main capillary flow towards the vertical wall is caused by the shear stress applied by the pressure gradient described by $Ca h^*(-\partial p^*/\partial x^*)$. The first term (S) in Eq. (4.7) describes the Marangoni effect

that corresponds to shear-stress due to the surface tension gradient that drives the fluid away from the vertical wall. The overall shear-stress on the bottom wall (Ca $\partial u^*/\partial z^*\,(z^*=0)$) then is the sum of these two terms.

The experimental S values in Fig. 4-4 for $\theta = 83^\circ$ and $\theta = 75^\circ$ are curve fitted with a polynomial of 6th order, as it provides the best coefficient of determination (R^2) among polynomials of different degrees (<8th order); this function is used to calculate $\mathrm{Ca}h^*(-\partial p^*/\partial x^*)$ and the overall non-dimensional shear stress on the horizontal wall from Eq. (4.7) at these two different contact angles; theses terms are both also shown in Fig. 4-4(a) and 4-4(b). The magnitudes of both S and $\mathrm{Ca}h^*(-\partial p^*/\partial x^*)$ change towards the vertical wall ($x^*=0$) resulting in separation at locations where the Marangoni term balances the pressure term leading to $\mathrm{Ca}\,\partial u^*/\partial z^*\,(z^*=0)=0$. At $\theta = 83^\circ$, as seen in Fig. 4-4(a), separation occurs only at $x^*_{sep} = 0.68$; however, with $\theta = 75^\circ$ separation occurs at three different locations ($x^*_{sep1} = 0.7, x^*_{sep2} = 1.59,\ x^*_{sep3} = 2.1$) as shown in Fig. 4-4(b). The measured separation point from micro-PIV analysis for $\theta = 83^\circ$ is $x^*_{sep} = 0.65$, and for $\theta = 75^\circ$ the separation points are $x^*_{sep1} = 0.67, x^*_{sep2} = 1.64,\ x^*_{sep3} = 2.19$ which confirms the theoretical approach. It is also clear from Fig. 4-4 that $S > 0$ is a necessary condition for flow separation; otherwise, $S \leq 0$ would be associated with a unidirectional flow towards the wall without flow separation.

The observed flow recirculation starts with one separation point near the vertical wall and as the contact angle decreases, new separation points cause additional recirculation away from the wall; however, Fig. 4-4(b) shows that the recirculation region at $x^*_{sep2} < x^* < x^*_{sep3}$ is associated with lower shear rates compared to the recirculating region near the wall $0 < x^* < x^*_{sep1}$. As a result, as S starts decreasing while the pressure gradient increases due to the surface curvature increase, the recirculation region away from the wall disappears before the one closest to the wall. Consequently, with further decrease in contact angle the recirculation regions disappear in sequence with respect to their distance from the vertical wall.

Although a microscope objective lens with a large field of view was used, the field of view was still limited and no more than two separation regions could be observed in our experiments; however, additional separation points can exist in theory at locations where the Marangoni stress balances the capillary pressure term.

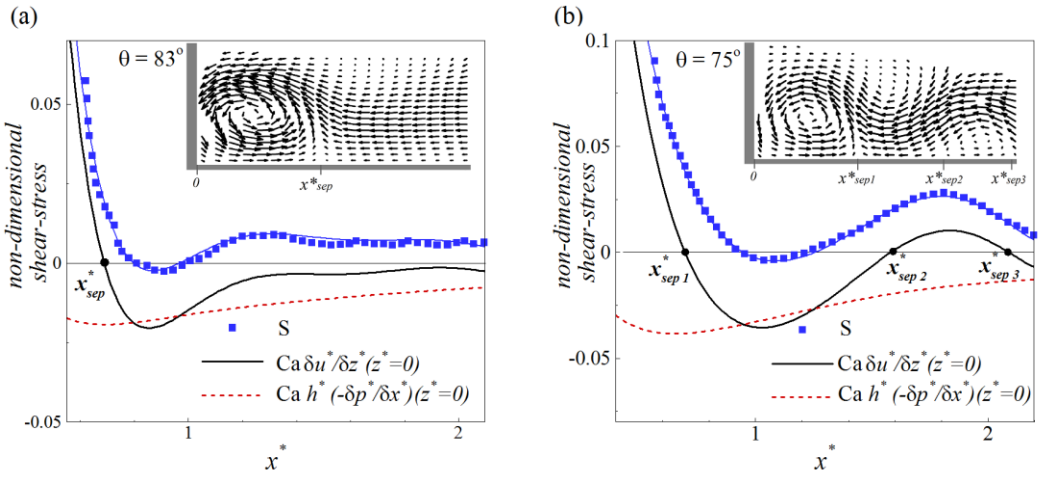

Figure 4-4 Non-dimensional shear stress on the horizontal wall with competing terms from Eq. (4.7) for an evaporating PVA solution with an initial concentration $C_0 = 18\%$ near a vertical wall with $H = 750\ \mu m$ and $b = 0.62$ at (a) $\theta = 83^{\circ}$ and (b) $\theta = 75^{\circ}$.

The separation locations predicted based on the proposed theory are in very good agreement with experimental results for $70^0 < \theta < 90^0$. For smaller contact angles ($\theta < 70^0$), a deviation is observed between theoretical and experimental values for the separation point locations. The deviation is expected since the analytical model is developed based on the simplifying assumption $(\partial h/\partial x)^2 \approx 0$ which is not valid as the slope of the free surface increases significantly for $\theta < 70^0$.

4.4 Conclusions

It is shown that flow separation can be caused by the Marangoni effect near a meniscus in conjunction with an evaporation-driven viscous capillary flow. The existence and locations of the flow separation/detachment points predicted by our

analytical model correlate well with experimental observations. The possible existence of such flow separation during thin film evaporation of a polymer solution is of high importance as it can affect the microstructure and local strength of the dried film [52]. The developed model adds to the known physical phenomena involved in the drying process of thin colloidal films, in addition to the extension of the flow separation theory to the creeping flow regime. While we partially applied experimental data to our theoretical model to predict the separation locations, a full CFD simulation of the problem could provide a fully independent prediction of the flow.

5 Summary and recommendations

5.1 Summary of key findings

5.1.1 Viscous flow recirculation

Under certain conditions the velocity fields from micro PIV revealed the existence of viscous vortices during the evaporation process. These vortices all show a similar time dependent behavior, as they appear soon after the beginning of the evaporation process in their maximum size, continuously shrink over time and finally disappear. The presence, size and endurance of these vortices were found to be influenced by the cavity depth and the initial polymer concentration. For initial concentrations $20\ wt\% < C_0 < 25\ wt\%$, the vortex is larger in deeper cavities while no vortices were observed with cavity depths smaller than $H = 300\ \mu m$. Increasing the initial polymer concentration also revealed a damping effect on the vortex size, as no vortices were observed with an initial concentration $C_0 > 25\ wt\%$, even in deepest cavities. The low Reynolds number ($Re < 10^{-5}$) during the evaporation process shows that inertia is negligible

compared to other forces. For the majority of the evaporation process, Marangoni stress and capillary forces are the two dominant forces and the competition between them determines the vortex size and endurance. The low initial polymer concentration correlates with higher capillary forces and sharper surface tension gradients at the free surface in addition to a higher evaporation time, which results in larger vortices for a longer time. Furthermore, by decreasing the cavity height, the evaporation time will also be decreased which reduces the vortex endurance as well.

Near the end of the evaporation process, the large increase of viscous forces, due to the viscosity increase, dampens the evaporation driven flow including the vortices.

5.1.2 Concentration field evolution

The concentration field was measured near the meniscus during the evaporation process using LIF. While the mean concentration increased over time, a concentration heterogeneity developed across the film. The surface concentration was higher compared to the bulk region throughout the drying process.

The effect of initial polymer concentration and the cavity depth on the concentration field were studied over time. Defining non-dimensional concentration ($C^* = C/C_0$), it was shown that the normalized concentration field

goes through a similar evolution during the evaporation time, regardless of initial concentration or cavity depth.

The capillary number at the surface was found to influence the surface concentration profile. A uniform concentration profile was observed at the surface with $Ca > 4 \cdot 10^{-5}$, while lower capillary numbers $Ca < 1 \cdot 10^{-5}$resulted in wavy patterns in the surface concentration profile. In fact, the viscous forces involved with larger capillary numbers were seen to have a damping effect on velocity disturbances at the surface, resulting in a more uniform surface concentration profile.

Comparing the velocity and concentration fields showed that at locations where significant recirculations exist, the concentration is lower and close to the initial concentration for an extended time. In fact, solvent molecules recirculating inside the vortex cannot exit the vortex due to low diffusion rates. As a result, the concentration stays locally constant inside the vortex.

5.1.3 Viscous flow separation

The momentum equations with thin-film and lubrication approximations were used to develop a mathematical model which can explain the observed recirculation inside the flow field. Since not all the governing equations could be solved analytically, experimental results were used to determine the missing parameters. For instance, the surface concentration data were used to determine

the surface tension gradient and the film thickness profile was determined by curve fitting of surface data points.

The theory supports that the competition between the two opposing flow generation mechanisms (capillary flow and Marangoni flow) results in a flow separation on the bottom wall of the cavity. The separation points were found using the developed model with the aid of our experimental data for fluid properties and concentration distribution. Results from the theoretical model were then compared with PIV results for separation point locations which revealed a very good agreement.

5.2 Major contributions

All contributions of this dissertation relate to

- It has been discovered that viscous vortices can be generated during the drying of polymer solutions inside a shallow well, in addition to the capillary flow and the Marangoni flow.
- The existence, size and duration of viscous vortices depend on geometrical parameters in addition to rheological parameters such as viscosity and surface tension.
- Regardless of initial polymer concentration or cavity height, the concentration field goes through a similar evolution during the evaporation process. As the concentration increases over time across the

film, while surface concentration remains higher locally. In addition, the concentration stays uniform locally inside the vortex.

- The competition between the capillary flow and the Marangoni flow can cause flow separation near the bottom wall of the cavity. This means the current theory on flow separation can be extended to the viscous flow regime.

5.3 Recommendations for future work

We studied the concentration field evolution and the effect of the velocity field on the concentration field during the drying process. A similar study can be performed on the structural properties evolution during the drying process. The effect of velocity field and drying process on the structural properties and degree of crystallization across the film are yet to be discovered.

The current study can be extended to other types of polymer solutions and different geometries. Drying of polymer solution droplets on a flat substrate is a related problem to be studied, as the drying process near the meniscus has not been reported yet for this geometry. The concentration measurement techniques introduced in this thesis, are expected to help with this problem as well. In addition, there is a different dependency of surface tension on polymer concentration for other polymer solutions. Thus, it will be interesting to study the drying process while the Marangoni flow's magnitude or direction is different.

The optical measurement techniques can be improved to acquire additional information from the flow field. Due to some shadow effects from the cavity side walls, it was not possible to measure the velocity and concentration at the close vicinity of the wall $x < \sim 0.2\ mm$. In addition, possible effects of optical errors on the velocity and concentration measurements can be studied.

Bibliography

[1] B.-J. de Gans, P. C. Duineveld, and U. S. Schubert, “Inkjet Printing of Polymers: State of the Art and Future Developments,” *Adv. Mater.*, vol. 16, no. 3, pp. 203–213, Feb. 2004.

[2] Y. Zheng, Z. He, Y. Gao, and J. Liu, “Direct Desktop Printed-Circuits-on-Paper Flexible Electronics,” *Sci Rep*, vol. 3, May 2013.

[3] H. Minemawari, T. Yamada, H. Matsui, J. Tsutsumi, S. Haas, R. Chiba, R. Kumai, and T. Hasegawa, “Inkjet printing of single-crystal films,” *Nature*, vol. 475, no. 7356, pp. 364–367, Jul. 2011.

[4] F.-C. Chen, J.-P. Lu, and W.-K. Huang, “Using ink-jet printing and coffee ring effect to fabricate refractive microlens arrays,” *Photonics Technol. Lett. IEEE*, vol. 21, no. 10, pp. 648–650, 2009.

[5] E. A. Sanchez, M. Waldmann, and C. B. Arnold, “Chalcogenide glass microlenses by inkjet printing,” *Appl. Opt.*, vol. 50, no. 14, pp. 1974–1978, 2011.

[6] U. Siemann, “Solvent cast technology – a versatile tool for thin film production,” in *Scattering Methods and the Properties of Polymer Materials*, vol. 130, Springer Berlin Heidelberg, 2005, pp. 1–14.

[7] S. Alsoy and J. L. Duda, “Modeling of multicomponent drying of polymer films,” *AIChE J.*, vol. 45, no. 4, pp. 896–905, Apr. 1999.

[8] F. L. Marten, “Vinyl Alcohol Polymers,” in *Encyclopedia of Polymer Science and Technology*, John Wiley & Sons, Inc., 2002.

[9] S.-H. Hyon, W.-I. Cha, Y. Ikada, M. Kita, Y. Ogura, and Y. Honda, “Poly(vinyl alcohol) hydrogels as soft contact lens material,” *J. Biomater. Sci. Polym. Ed.*, vol. 5, no. 5, pp. 397–406, Jan. 1994.

[10] I. Mansoor, U. O. Hafeli, and B. Stoeber, “Hollow Out-of-Plane Polymer Microneedles Made by Solvent Casting for Transdermal Drug Delivery,” *J. Microelectromechanical Syst.*, vol. 21, no. 1, pp. 44–52, Feb. 2012.

[11] S. Ghoshal, P. Denner, S. Stapf, and C. Mattea, “Study of the Formation of Poly(vinyl alcohol) Films,” *Macromolecules*, vol. 45, no. 4, pp. 1913–1923, Feb. 2012.

[12] B. Briscoe, P. Luckham, and S. Zhu, “The effects of hydrogen bonding upon the viscosity of aqueous poly(vinyl alcohol) solutions,” *Polymer*, vol. 41, no. 10, pp. 3851–3860, May 2000.

[13] P. Molyneux, *Water-soluble synthetic polymers: properties and behavior*. CRC Press. Inc., 1983.

[14] J. Tao, “Effects of Molecular weight and Solution Concentration on Electrospinning of PVA,” Worcester Polytechnic Institute, 2003.

[15] H.-W. Gao, R.-J. Yang, J.-Y. He, and L. Yang, “Rheological behaviors of PVA/H2O solutions of high-polymer concentration,” *J. Appl. Polym. Sci.*, vol. 116, no. 3, pp. 1459–1466, May 2010.

[16] M. Bercea, S. Morariu, and D. Rusu, “In situ gelation of aqueous solutions of entangled poly(vinyl alcohol),” *Soft Matter*, vol. 9, no. 4, pp. 1244–1253, 2013.

[17] E. Levänen, T. Mäntylä, P. Mikkola, and J. B. Rosenholm, “Influence of Additives on Capillary Absorption of Aqueous Solutions into Asymmetric Porous Ceramic Substrate,” *J. Colloid Interface Sci.*, vol. 234, no. 1, pp. 28–34, Feb. 2001.

[18] G. O. Yahya, S. K. Asrof Ali, and E. Z. Hamad, “Surface and interfacial activities of hydrophobically modified poly(vinyl alcohol) (PVA),” *Polymer*, vol. 37, no. 7, pp. 1183–1188, Mar. 1996.

[19] M. Okazaki, K. Shioda, K. Masuda, and R. Toei, “Drying mechanism of coated film of polymer solution,” *J. Chem. Eng. Jpn.*, vol. 7, no. 2, pp. 99–105, 1974.

[20] J. S. Vrentas and C. M. Vrentas, “Drying of solvent-coated polymer films,” *J. Polym. Sci. Part B Polym. Phys.*, vol. 32, no. 1, pp. 187–194, Jan. 1994.

[21] E. Ciampi and P. J. McDonald, “Skin Formation and Water Distribution in Semicrystalline Polymer Layers Cast from Solution: A Magnetic Resonance Imaging Study,” *Macromolecules*, vol. 36, no. 22, pp. 8398–8405, Nov. 2003.

[22] S. Ghoshal, P. Denner, S. Stapf, and C. Mattea, “Structural and dynamical heterogeneities in PVA films induced by evaporation during the formation process,” *Chem. Phys. Lett.*, vol. 515, no. 4, pp. 231–234, 2011.

[23] S.-S. Wong, S. A. Altinkaya, and S. K. Mallapragada, “Understanding the effect of skin formation on the removal of solvents from semicrystalline polymers,” *J. Polym. Sci. Part B Polym. Phys.*, vol. 43, no. 22, pp. 3191–3204, Nov. 2005.

[24] J. Eggers and L. M. Pismen, “Nonlocal description of evaporating drops,” *Phys. Fluids*, vol. 22, no. 11, p. 112101, Nov. 2010.

[25] R. D. Deegan, O. Bakajin, T. F. Dupont, G. Huber, S. R. Nagel, and T. A. Witten, “Capillary flow as the cause of ring stains from dried liquid drops,” *Nature*, vol. 389, no. 6653, pp. 827–829, Oct. 1997.

[26] R. D. Deegan, O. Bakajin, T. F. Dupont, G. Huber, S. R. Nagel, and T. A. Witten, “Contact line deposits in an evaporating drop,” *Phys. Rev. E*, vol. 62, no. 1, p. 756, 2000.

[27] P. J. Yunker, T. Still, M. A. Lohr, and A. G. Yodh, “Suppression of the coffee-ring effect by shape-dependent capillary interactions,” *Nature*, vol. 476, no. 7360, pp. 308–311, Aug. 2011.

[28] X. Shen, C.-M. Ho, and T.-S. Wong, “Minimal Size of Coffee Ring Structure,” *J. Phys. Chem. B*, vol. 114, no. 16, pp. 5269–5274, Apr. 2010.

[29] H. Hu and R. G. Larson, “Marangoni Effect Reverses Coffee-Ring Depositions,” *J. Phys. Chem. B*, vol. 110, no. 14, pp. 7090–7094, Apr. 2006.

[30] I. Mansoor and B. Stoeber, “PIV measurements of flow in drying polymer solutions during solvent casting,” *Exp. Fluids*, vol. 50, no. 5, pp. 1409–1420, May 2011.

[31] T. Kajiya and M. Doi, “Dynamics of Drying Process of Polymer Solution Droplets: Analysis of Polymer Transport and Control of Film Profiles,” *Nihon Reoroji Gakkaishi*, vol. 39, no. 1_2, pp. 17–28, 2011.

[32] S. G. Yiantsios and B. G. Higgins, “Marangoni flows during drying of colloidal films,” *Phys. Fluids*, vol. 18, no. 8, p. 082103, Aug. 2006.

[33] P. Chamarthy, H. K. Dhavaleswarapu, S. V. Garimella, J. Y. Murthy, and S. T. Wereley, “Visualization of convection patterns near an evaporating meniscus using μPIV,” *Exp. Fluids*, vol. 44, no. 3, pp. 431–438, Mar. 2008.

[34] C. Buffone, C. Minetti, L. Boussemaere, M. Roudgar, and J. De Coninck, "Marangoni convection in evaporating meniscus with changing contact angle," *Exp. Fluids*, vol. 55, no. 10, pp. 1–8, 2014.

[35] E. M. Furst, "Applications of laser tweezers in complex fluid rheology," *Curr. Opin. Colloid Interface Sci.*, vol. 10, no. 1–2, pp. 79–86, Aug. 2005.

[36] K. Sakai and Y. Yamamoto, "Electric field tweezers for characterization of liquid surface," *Appl. Phys. Lett.*, vol. 89, no. 21, p. 211911, 2006.

[37] Y. Komoda, L. G. Leal, and T. M. Squires, "Local, Real-Time Measurement of Drying Films of Aqueous Polymer Solutions Using Active Microrheology," *Langmuir*, vol. 30, no. 18, pp. 5230–5237, May 2014.

[38] H. K. Moffatt, "Viscous and resistive eddies near a sharp corner," *J. Fluid Mech.*, vol. 18, no. 01, pp. 1–18, 1964.

[39] S. Taneda, "Visualization of separating Stokes flows," *J. Phys. Soc. Jpn.*, vol. 46, no. 6, pp. 1935–1942, 1979.

[40] M. Scholle, A. Wierschem, and N. Aksel, "Creeping films with vortices over strongly undulated bottoms," *Acta Mech.*, vol. 168, no. 3–4, pp. 167–193, 2004.

[41] M. Scholle, A. Haas, N. Aksel, M. Wilson, H. Thompson, and P. Gaskell, "Competing geometric and inertial effects on local flow structure in thick gravity-driven fluid films," *Phys. Fluids*, vol. 20, no. 12, p. 123101, 2008.

[42] A. Wierschem, M. Scholle, and N. Aksel, "Vortices in film flow over strongly undulated bottom profiles at low Reynolds numbers," *Phys. Fluids*, vol. 15, no. 2, pp. 426–435, 2003.

[43] M. S. N. Oliveira, F. T. Pinho, and M. A. Alves, "Divergent streamlines and free vortices in Newtonian fluid flows in microfluidic flow-focusing devices," *J. Fluid Mech.*,

vol. 711, pp. 171–191, 2012.

[44] R. Fishler, M. K. Mulligan, and J. Sznitman, “Mapping low-Reynolds-number microcavity flows using microfluidic screening devices,” *Microfluid. Nanofluidics*, vol. 15, no. 4, pp. 491–500, 2013.

[45] R. I. Tanner and K. Walters, *Rheology: an historical perspective*, vol. 7. Elsevier, 1998.

[46] Rui Lima and Shigeo Wada and Ken-ichi Tsubota and Takami Yamaguchi, “Confocal micro-PIV measurements of three-dimensional profiles of cell suspension flow in a square microchannel,” *Meas. Sci. Technol.*, vol. 17, no. 4, p. 797, 2006.

[47] A. Babaie and B. Stoeber, “Concentration Field Evolution during the Drying of a Thin Polymer Solution Film near the Contact Line,” *Langmuir*, vol. 31, no. 33, pp. 9033–9040, Aug. 2015.

[48] B. R. Munson, D. F. Young, and T. H. Okiishi, *Fundamentals of Fluid Mechanics*, 4th ed. New York: Wiley, 2002.

[49] L. E. Rodd, T. P. Scott, D. V. Boger, J. J. Cooper-White, and G. H. McKinley, “The inertio-elastic planar entry flow of low-viscosity elastic fluids in micro-fabricated geometries,” *J. Non-Newton. Fluid Mech.*, vol. 129, no. 1, pp. 1–22, Aug. 2005.

[50] M. A. Alves, F. T. Pinho, and P. J. Oliveira, “Viscoelastic flow in a 3D square/square contraction: Visualizations and simulations,” *J. Rheol. 1978-Present*, vol. 52, no. 6, pp. 1347–1368, Nov. 2008.

[51] M. Scholle, A. Haas, N. Aksel, M. Wilson, H. Thompson, and P. Gaskell, “Eddy genesis and manipulation in plane laminar shear flow,” *Phys. Fluids*, vol. 21, no. 7, p. 073602, 2009.

[52] A. Babaie, S. Madadkhani, and B. Stoeber, “Evaporation-driven low Reynolds number vortices in a cavity,” *Phys. Fluids*, vol. 26, no. 3, p. 033102, Mar. 2014.

[53] M. B. Shafii, C. Lum, and M. Koochesfahani, “In situ LIF temperature measurements in aqueous ammonium chloride solution during uni-directional solidification,” *Exp. Fluids*, vol. 48, no. 4, pp. 651–662, Apr. 2010.

[54] J. P. Crimaldi, “Planar laser induced fluorescence in aqueous flows,” *Exp. Fluids*, vol. 44, no. 6, pp. 851–863, Jun. 2008.

[55] C. T. Culbertson, S. C. Jacobson, and J. Michael Ramsey, “Diffusion coefficient measurements in microfluidic devices,” *Talanta*, vol. 56, no. 2, pp. 365–373, Feb. 2002.

[56] M. O. Ngui and S. K. Mallapragada, “Quantitative analysis of crystallization and skin formation during isothermal solvent removal from semicrystalline polymers,” *Polymer*, vol. 40, no. 19, pp. 5393–5400, Sep. 1999.

[57] B. J. Fischer, “Particle Convection in an Evaporating Colloidal Droplet,” *Langmuir*, vol. 18, no. 1, pp. 60–67, Jan. 2002.

[58] A. Babaie and B. Stoeber, “Viscous flow separation caused by the Marangoni effect in competition with capillary flow,” *Phys. Fluids*, vol. 27, no. 7, p. 071702, Jul. 2015.

[59] P. H. Gaskell, P. K. Jimack, M. Sellier, and H. M. Thompson, “Flow of evaporating, gravity-driven thin liquid films over topography,” *Phys. Fluids*, vol. 18, no. 1, p. 013601, Jan. 2006.

[60] P. C. Wayner Jr., Y. K. Kao, and L. V. LaCroix, “The interline heat-transfer coefficient of an evaporating wetting film,” *Int. J. Heat Mass Transf.*, vol. 19, no. 5, pp. 487–492, May 1976.

[61] L. Espín and S. Kumar, “Sagging of Evaporating Droplets of Colloidal Suspensions on Inclined Substrates,” *Langmuir*, vol. 30, no. 40, pp. 11966–11974, 2014.

[62] L. W. Schwartz, D. E. Weidner, and R. R. Eley, “An Analysis of the Effect of Surfactant on the Leveling Behavior of a Thin Liquid Coating Layer,” *Langmuir*, vol. 11, no. 10, pp. 3690–3693, Oct. 1995.

[63] H. Wang, S. V. Garimella, and J. Y. Murthy, “Characteristics of an evaporating thin film in a microchannel,” *Int. J. Heat Mass Transf.*, vol. 50, no. 19–20, pp. 3933–3942, Sep. 2007.

[64] A. F. Routh, “Drying of thin colloidal films,” *Rep. Prog. Phys.*, vol. 76, no. 4, p. 046603, Apr. 2013.